ISSN Print : 2320-2092, Online : 2321-2071

International Journal of Mechanical & Production Engineering (IJMPE)

Volume No. 12
Issue No. 1
January - April 2024

ENRICHED PUBLICATIONS PVT. LTD

S-9, IInd FLOOR, MLU POCKET,
MANISH ABHINAV PLAZA-II, ABOVE FEDERAL BANK,
PLOT NO-5, SECTOR-5, DWARKA, NEW DELHI, INDIA-110075,
PHONE: - + (91)-(11)-47026006

ISSN Print : 2320-2092, Online : 2321-2071

International Journal of Mechanical & Production Engineering (IJMPE)

Aim & Scope

The International Journal of Mechanical & Production Engineering (IJMPE) is an international forum for the publication and dissemination of original work which contributes to greater scientific understanding of the main disciplines underpinning the whole spectrum of mechanical engineering, which includes, but is not limited to, Materials and Design Engineering, Production Engineering and Fusion Technology, Dynamics, Vibration and Control, Thermal Engineering and Fluids Engineering, Environmental protection, etc..

The IJMPE is a peer-reviewed open access journal published monthly in English-language. Only original, innovative and novel papers will be considered for publication in the International Journal of Mechanical Sciences and before considering their work, authors are required to confirm that their paper has not been submitted to any other journal in English or any other language. Original ideas may be discussed in advance with the Editor (mail: Info.Ijmpe@Gmail.Com), to clear the ground for a draft submission. All papers are then peer reviewed by relevant experts and feedback is given whether or not a paper is accepted or returned for further work. The Editor's policy is to try and accommodate contributions of all sizes above the minimum threshold where length is dictated by the needs of the subject matter.

The Journal can be found from the official URL www.ijmpe.iraj.in

ISSN Print : 2320-2092, Online : 2321-2071

Chief Editor

Editor

Associate Editor

Managing Editor

Editorial Board

ISSN Print : 2320-2092, Online : 2321-2071

International Journal of Mechanical & Production Engineering (IJMPE)

(Volume No. 12, Issue No. 1, January - April 2024)

Contents

ISSN Print : 2320-2092, Online : 2321-2071

Finite Element Modeling of the Hot Ultrasonic Assisted Turning of Titanium Alloy in Terms of Different Vibrational Parameters

[1] Melih Cemal Kuşhan, [2] Sezan Orak, [3] M. Alper Sofuoğlu
Department of Mechanical Engineering, Eskişehir Osmangazi University, 26480, Eskişehir, Turkey
E-mail: [1]mkushan@ogu.edu.tr

ABSTRACT

In this study, Hot Ultrasonic Assisted Turning (HUAT) of Ti6Al4V alloy was studied numerically via DEFORM- 2D software. This novel machining method combines Ultrasonic Assisted Turning (UAT) and hot machining operations. Vibrational parameters were chosen as cutting parameters for the simulation study. Cutting forces, maximum effective stresses, and cutting temperatures were calculated with respect to these parameters.

Keywords - Hot Machining, Cutting Forces, Vibration, Ultrasonic Assisted Machining, Power Consumption

I. INTRODUCTION

In recent years, titanium alloys have wide range of applications in automotive, aerospace and biomedical sectors [18]. These materials have superior strength and remarkable corrosion resistance at high temperatures. In addition, the low density of these materials make the weight reduction in structures. However, machining of titanium alloys is still difficult due to their high hardness, deep chemical affinity, and lower thermal conductivity. Recent investigations have been carried out by using several manufacturing techniques to prevent the poor machinability of these materials [1]. Ultrasonic Assisted Turning (UAT) is an intermittent machining operation based on vibrations produced by an ultrasonic setup. In the literature, different studies have been performed to observe the UAT method. Several studies suggested models for predicting workpiece surface roughness [2-5] and surface texture based on vibration characteristics [6-11]. Also, different analytical-numerical studies were carried out [12-13]. In order to minimize cutting forces, an ultrasonic-based vibrational cutting system was used [14]. In this study, HUAT method was numerically investigated to find appropriate cutting parameters. A parametric study was carried out. A titanium alloy (Ti6Al4V) was chosen as a workpiece. Vibrational parameters were used as cutting parameters in the simulations. An experimental study was carried out to validate the developed model. Cutting forces and chip thickness were used to compare the results.

II. NUMERICAL STUDY

2D finite element model was developed in the DEFORM-2D program. Lagrange FE formulation was used. Dry machining condition was used. Ti6Al4V was used as the workpiece. Johnson Cook material

model was used to model the workpiece. The equations of the model are shown below (Eqs. 1-2). Table 1 presents the value of coefficients for this model. The material of the cutting tool is WC + TiAlN with rake and clearance angles, 00 and 70, respectively. The Cockcroft and Latham fracture criterion was used and the coefficient is taken as 100. Both shear and coulomb frictions were selected with the range of 0.5-1. Material properties for Ti6Al4V have been determined using the literature [15]. Friction models, friction zones, and coefficients were obtained using different trials and a literature study [15]. The vibration was applied in the cutting direction. Vibration amplitudes range from 2 to 15 microns, and vibration frequencies are between 17-24 kHz. The other cutting parameters were kept constant (pre-heating temperature 100 0C, Cutting speed = 40 m/min, Feed rate = 0.1 mm / rev.).

$$\sigma = \left(A + B\varepsilon^{n}\right)\left(1 + C\ln\left(\frac{\dot{\varepsilon}}{\dot{\varepsilon}_0}\right)\right)\left(1 - T^{*}\right)^{m} \quad (1)$$

$$T^{*} = \frac{\left(T - T_{room}\right)}{\left(T_{melt} - T_{room}\right)} \quad (2)$$

$\frac{\dot{\varepsilon}}{\dot{\varepsilon}_0}$: Plastic strain rate/reference plastic strain rate.

n: Sensitivity of strain rate for material.

T_{room}: Room temperature.

T_{melt}: Melting temperature of the material.

A, B, C, m : The constants of material.

Material	A(Mpa)	B(Mpa)	C	n	m	*e* 0
Ti6Al4	724.7	683.1	0.03	0.4	1	200

Table 1. The coefficients of the Johnson - cook model for Ti6A14V [16]

III. RESULTS AND DISCUSSION

3.1. The Results of the Simulation Study

Cutting forces, max. effective stresses and max. cutting temperature do not change significantly when the vibrational amplitude or frequency changes. Tables 2-3 give the average cutting forces, maximum effective stresses, and cutting temperatures for different vibration amplitudes and frequencies. Figure 1 shows the cutting temperature distribution for 17 kHz vibration. When the amplitude of vibration increase, the extent of separation between the tool and workpiece in one complete cycle increase, which causes a higher force reduction in HUAT. It was obtained that the higher vibration amplitude causes an increase in a force reduction. At lower frequency, the tool separation is slow which accelerated with an increase in the frequency in HUAT. Increasing vibration frequency and amplitude causes higher cutting temperatures. The results of the study are compatible with the literature [17].

Amplitude (micron)	F_x (N)	F_y (N)	Maximum effective stress (MPa)	Maximum cutting temperature (^{0}C)
15	97.5	33.0	1930~1830	652~580
10	101.0	34.52		
8	102.0	36.82		
2	107.5	40.32		

Table 2. Average cutting forces, maximum effective stresses and maximum cutting temperatures with respect to the different vibration amplitudes (Vibration frequency=20 kHz)

Frequency (kHz)	F_x (N)	F_y (N)	Maximum effective stress (MPa)	Maximum cutting temperature (^{0}C)
24	104.7	38.32	1930~1630	730~593
19	107.5	39.5		
17	111.2	46.8		

Table 3. Average cutting forces, maximum effective stresses and maximum cutting temperatures with respect to the different vibration frequency (Vibration amplitude=20 microns)

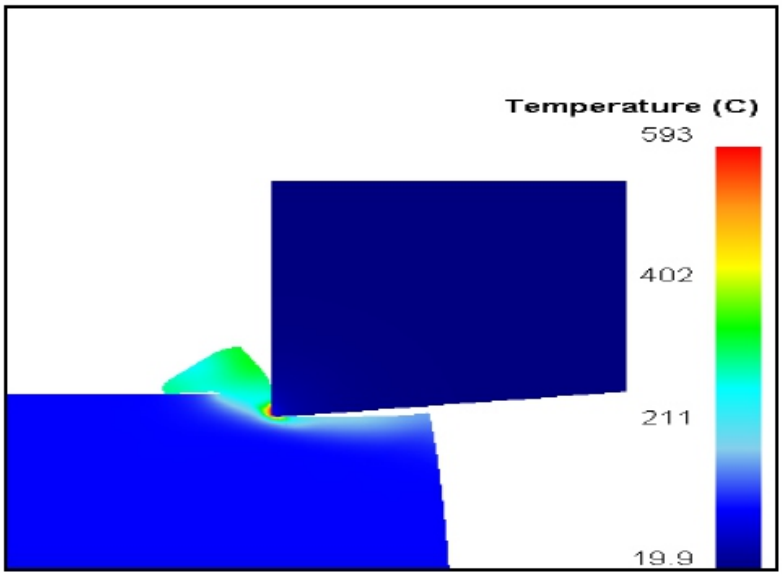

Figure 1. Cutting temperature distribution for 17 kHz vibration.

3.2. Experimental Study

In this stage, a universal lathe was used as shown in Figure 2. Figure 3 shows the cutting tool used. The frequency of the ultrasonic system was 20 kHz, and the amplitude was measured as 20 μm using a dial indicator. A thermal camera was used to measure the cutting tool temperature. A thermocouple was also used to control the temperature.

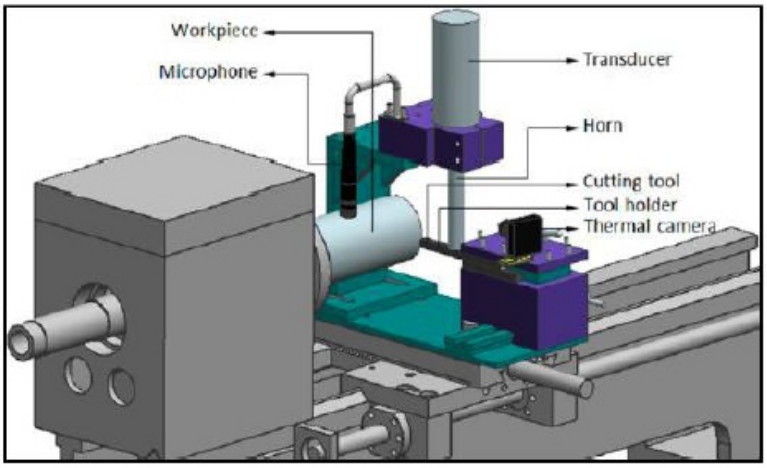

Figure 2. Ultrasonic assisted turning setup

Figure 3. The cutting tool used in the experiments

The validation experiment was performed at 20^0C for ultrasonic assisted turning. Cutting speed was 40 m/min. Experimental and simulation studies were compared in terms of cutting tool temperatures and average chip thicknesses. Table 2 displays the results. It was obtained that the experimental results are consistent with the simulation study.

	Cutting tool temperatures (^{0}C)	Average chip thickness (mm)
Experimental study	235.30	0.27
Numerical study	252.45	0.23

Table 2. Comparison of experimental and simulation studies

IV. CONCLUSION

In this research, a simulation study was performed for a new turning method (Hot ultrasonic assisted turning). Ti6Al4V alloy was used as workpiece material. Amplitude and frequency of vibration were used as inputs. Vibrational parameters do not affect cutting forces, max. effective stress and cutting temperatures significantly. However, as the amplitude of vibration increased, the extent of separation between the tool and workpiece in one complete cycle increased, which causes force reduction in hot ultrasonic assisted turning. It was seen that the higher vibration amplitude give rise to an increase in the force reduction. The proposed experimental study is useful to understand the effects of HUAT. In future studies, different cutting parameters (tool geometry, etc.) might be investigated. Also, various materials can be tried in the simulation studies.

ACKNOWLEDGMENT

This work was supported by the Scientific Research Projects Commission of Eskişehir Osmangazi University as project number 2018/15C102.

REFERENCE

[1] S. A. Niknam, R. Khettabi, and V. Songmene, "Machinability and Machining of Titanium Alloys: A Review," in Machining of Titanium Alloys, J. P. Davim, Ed. Berlin, Heidelberg: Springer Berlin Heidelberg, 1–30, 2014

[2] E. Shamoto, N. Suzuki, and R. Hino, "Analysis of 3D elliptical vibration cutting with thin shear plane model," CIRP Ann. - Manuf. Technol., 57 (1), 57–60, 2008.

[3] E. Shamoto and T. Moriwaki, "Study on Elliptical Vibration Cutting," CIRP Ann. - Manuf. Technol., 43 (1), 35–38, 1994.

[4] C. F. Cheung and W. B. Lee, "Modelling and simulation of surface topography in ultra-precision diamond turning," Proc. Inst. Mech. Eng. Part B J. Eng. Manuf., 214 (6), 463–480, 2000.

[5] D.S. Kim, I.C. Chang, and S.W. Kim, "Microscopic topographical analysis of tool vibration effects on diamond turned optical surfaces," Precis. Eng., 26 (2), 168–174, 2002.

[6] S. A. Sajjady, H. Nouri Hossein Abadi, S. Amini, and R. Nosouhi, "Analytical and experimental study of topography of surface texture in ultrasonic vibration assisted turning," Mater. Des., 93, 311–323, 2016.

[7] C. Zhang, K. Ehmann, and Y. Li, "Analysis of cutting forces in the ultrasonic elliptical vibration-assisted micro-groove turning process," Int. J. Adv. Manuf. Technol., 78, (1–4), 139–152, 2015.

[8] P. Guo and K. F. Ehmann, "Development of a tertiary motion generator for elliptical vibration texturing," Precis. Eng., 37 (2), 364–371, 2013.

[9] C. Zhang, P. Guo, K. F. Ehmann, and Y. Li, "Effects of ultrasonic vibrations in micro-groove turning," Ultrasonics, 67, 30–40, 2016.

[10] S. Amini, H. N. Hosseinabadi, and S. A. Sajjady, "Experimental study on effect of micro textured surfaces generated by ultrasonic vibration assisted face turning on friction and wear performance," Appl. Surf. Sci., 390, 633–648, 2016.

[11] V. V. Silberschmidt, S. M. A. Mahdy, M. A. Gouda, A. Naseer, A. Maurotto, and A. Roy, "Surface-roughness Improvement in Ultrasonically Assisted Turning," Procedia CIRP, 13, 49–54, 2014.

[12] X. Zhang, A. Senthil Kumar, M. Rahman, C. Nath, and K. Liu, "An analytical force model for orthogonal elliptical vibration cutting technique," J. Manuf. Process., 14 (3), 378–387, 2012.

[13] X. Zhang, A. S. Kumar, M. Rahman, and K. Liu, "Modeling of the effect of tool edge radius on surface generation in elliptical vibration cutting," Int. J. Adv. Manuf. Technol., 65, (1–4), 35–42, 2013.

[14] H. Razavi and M. Mirbagheri, "Design and fabrication of a novel vibrational system for ultrasonic assisted oblique turning process," J. Mech. Sci. Technol., 30 (2), 827–835, 2016.

[15] T. Özel, M. Sima, AK Srivastava, "Finite element simulation of high-speed machining Ti-6Al-4V alloy using modified material models." Trans NAMRI/SME 38:49–56, 2010

[16] W.S. Lee, C.F. Lin "Plastic deformation and fracture behavior of Ti–6Al–4V alloy loaded with high strain rate under various temperatures" Mater Sci Eng A 241(1–2):48–59, 1998

[17] R. Muhammad, "Hot ultrasonically assisted turning of Ti15V3Al3Cr3Sn: experimental and numerical analysis," Doctoral Thesis, Loughborough University, UK, 2013

[18] M. A. Sofuoğlu, F. H. Çakır, M.C. Kuşhan, S. Orak, S. Gürgen, "Numerical Investigation of Hot Ultrasonic Assisted Turning of Titanium Alloy", 3rd International Conference on Engineering and Natural Sciences (ICENS 2017), May 3 to 7, Budapest, Hungary, 2017

ISSN Print : 2320-2092, Online : 2321-2071

Alkali-Activated Mortars for Sustainable Construction Material: Effects of Binder - to - aggregate Ratio and Curing Conditions

[1] Manfredi Saeli, [2] Maria Paula Seabra, [3] Joao A. Labrincha
Department of Materials and Ceramics Engineering (DEMAC), Aveiro Institute of Materials (CICECO) University of Aveiro, 3810-193 Aveiro, Portugal
E-mail: [1]manfredi.saeli@ua.pt / manfredi.saeli@gmail.com, [2]pseabra@ua.pt, [3]jal@ua.pt

ABSTRACT

Valorisation and reuse of industrial wastes has become a worldwide compelling topic to improve the sustainability of processes and materials. This paper discusses an alternative way to recycle the biomass fly ash, generated by the kraft pulp industry, to manufacture novel geopolymeric mortars intended for applications in construction. Biomass fly ash was used as a raw material, in partial substitution of the commonly used metakaolin, natural siliceous sand as aggregate. The followed manufacture process is highly simple and reproducible. Various proportions binder to aggregate were tested to study the effect on the final mortars properties. The mortars mechanical resistance was also studied in relation to the temperature and duration of curing in order to define the best condition to gain the maximum mechanical resistance. Also submersed curing was tested. Moreover, the mechanical performance was investigated under the effect of natural ageing. The investigations indicate that the novel mortars can be used as structural material in construction and represent an efficient solution to reduce the environmental footprint associated with waste disposal in light of the circular economy.

Keywords - Construction, Mortar, Geopolymer, Biomass fly ash, Pulp-paper industry, Waste, Circular economy.

I. INTRODUCTION

In the last XX century, many concerns started to arise on environmental and socio-economic issues such as depletion of natural resources, climate change, and atmospheric pollution. Then, both the public and private sectors, pushed over by a pressing public opinion, started to discuss on the most convenient way to improve the worldwide industrial development in a sustainable and effective way.

The circular economy is intended as the most accredited economic model addressing the issues of environmental depletion and long-term economic growth and stability, strictly coupled with social equity. In accordance, the circular industrial management, from manufacture to disposal, has started to be considered a viable and cost-effective solution to improve the industrial systems. Valorisation, reuse, and recycle of trashes, wastes, by-products, and end-of-cycle products have then become a real and increasing business [1, 2].

Transforming wastes into novel and useful products is becoming highly important. Indeed, many economic sectors, as construction, are facing the expanding problem of wastes and by-products treatment and disposal, that yearly generates an incredible loss of financial resources. Then, new technologies are investigated to transform low-quality, zero- or low-cost materials into high-value products with a surplus of financial resources and a consequent reduction in environmental impact associated with human activities.

This paper investigates the production of green geopolymeric (GP) mortars, formulated with industrial waste, and mainly intended for applications in civil engineering and architecture. GP are inorganic alkali-activated binders made of a reactive solid alumina-silicate source interacting with an alkaline solution [3]. Nowadays, GP are considered the most viable and green alternative to the Ordinary Portland Cement [4, 5].

In this work, the common source of aluminium and silicon, metakaolin (MK), was partially substituted by biomass fly ash (BFA), making the GP more sustainable. The used BFA derives from a local Kraft paper-pulp industry. The Kraft process involves the digestion of lignin by an alkaline mixture of sodium hydroxide, sodium sulfide, and water [6]. During such process, the BFA is produced in the biomass boiler employed for energy production at mill site and collected at the electrostatic precipitator as waste [7]. Here, the BFA is recycled and used to substitute the MK with a rate of 70 wt.%, generating a high environmental drawback [8, 9].

This work details the effects of binder-to-aggregate ratio (mix design), various curing conditions (temperature, duration, and medium), and natural ageing to study the long-term performance and durability of the studied GP-mortars. Moreover, it offers a valid alternative to traditional disposal suggesting a methodology to manufacture a new class of novel green construction materials intended for a global market.

II. EXPERIMENTAL DETAILS

2.1. Raw materials

In this work the GP-binder was designed with the following oxides ratios: SiO_2/Al_2O_3 = 5.27, Na_2O/Al_2O_3 = 1.31, Na_2O/SiO_2 = 0.25, and $H_2O/Na2O$ = 15.9, according to [8].

The tested formulation uses a mixture of BFA (70 wt.%) and MK (30 wt.%) as a solid source of alumina and silica. Benchmark MK is purchased as Argical™ from Univar® and used to adjust the GP desired

molar oxide ratios. BFA was supplied by a local Kraft pulp industry and presents α–quartz, calcite, mica group mineral (mixture of muscovite/illite), and microcline as main crystalline phases.

The alkaline activation was achieved by using a solution of sodium silicate (H_2O = 62.1 wt.%; SiO_2/Na_2O = 3.15; Quimialmel, D40-PQ) and sodium hydroxide (ACS reagent, 97%; Honeywell). The NaOH solution (10 M) was prepared by dissolving the sodium hydroxide pellets in distilled water at least 24 h prior to use. The used molarity was selected based on the cited previous work.

The natural siliceous sand used as fine aggregate was furnished by Saint-Gobain Weber Portugal.

The main characteristics of the produced GP-binder are: ratio water/cement - 0.78; bulk density - 1307 Kg/m^3; sorptivity by immersion – 38 %; coefficient of capillarity - 0.87 $kg/(m^2 \cdot min0.5)$; uniaxial compressive strength - 22.15 ± 1.22 Mpa.

2.2. Manufacture process

GP-mortar specimens were prepared according to EN 998-2:2016, adapting the common procedure used for traditional cement-based mortars.

Mortar manufacture consisted of [9]: (I) dry mixing of MK and BFA to ensure a uniform blend for 1 min; (II) homogenisation of sodium hydroxide and silicate at 50 rpm for 5 min; (III) mixing of the alkaline solution with the solid precursors at 60 rpm for 9 min; (IV) adding the sand and mixing for 1 min to ensure homogeneity. The fresh slurry was poured into standard metallic moulds (40×40×160 mm) and vibrated for 2 min on a vibrating table to achieve compactness, and remove entrained air. Then, the moulds were sealed with a plastic film for 24 hr to prevent water evaporation until the specimens were hardened. Finally, the moulds were unsealed, the specimens demoulded and cured until testing.

2.3. Materials characterisation

The consistency (spread) of the fresh GP-mortars was estimated by flow table testing according to EN 1015- 3:1999. Bulk density (geometrical) was calculated as the average of three specimens. The water absorption was determined by the Archimedes principle (weight variation, ΔP/P, %); the capillary coefficient (C) according to EN 1015-18. Three replicas were used to calculate the mean values for the two sorptivity tests. The mechanical performance was determined according to EN 1015-11 and EN 998-2 by means of the uniaxial compressive strength (UCS) test. A universal testing machine (Shimadzu, AG-25TA), provided with a 250 kN load cell, running at 0.5 mm/min displacement rate, was used. The software that returned the measured load and strain values was Trapezium v. 1.2.4. The mean

values were obtained from three tests randomly taken from the sample batch. Axial strain (ε) was also calculated as specimens height variation (ΔL/L, %).

2.4. Mortars mix design and curing conditions

This scientific study is formally divided in various steps to evaluate the most efficient mix design and the most effective curing conditions.

Step – 1: Mortars were produced by adding the aggregate (sand) in five proportions, binder/aggregate ratio (B/A), in order to evaluate the influence on the GP-mortars final properties. The tested GP-mortar formulations (mix design) are shown in Table 1. Here the liquid/solid (L/S) ratio and the measured consistency (flow table test) are also reported. The five formulations were cured at ambient conditions (20 °C, 65% RH) and tested at the 28th day of curing. This procedure avoids any supply of external heat and, consequently, generates a more sustainable and cost effective process. This task will allow to define the best mix design intended for applications in construction.

Specimen	Ratio		Spread [cm]
	B/A	L/S	
1	1:1	0.391	>30
2	1:2	0.261	26
3	1:3	0.196	21
4	1:4	0.156	15
5	1:5	0.130	10

Table 1: Mortars mix design

The most suitable mix design (that resulted the one with ratio B/A equal to 1:3) was then used for the following steps. Those foresee the curing at different temperatures and durations to understand if (and eventually how) temperature and duration of curing influence the final mechanical resistance (UCS).

Step – 2: Specimens were cured at different temperatures, following two procedures: (I) curing at constant temperature in a climatic chamber for 28 days; (II) curing at constant temperature in a climatic chamber for the first day; then at ambient conditions (20°C) for 27 days. The curing humidity (RH) has been kept constant at 65% (ambient humidity).

Step – 3: Specimens were cured, from the first moment, into water (distilled and salty), to simulate possible applications for submersed structures.

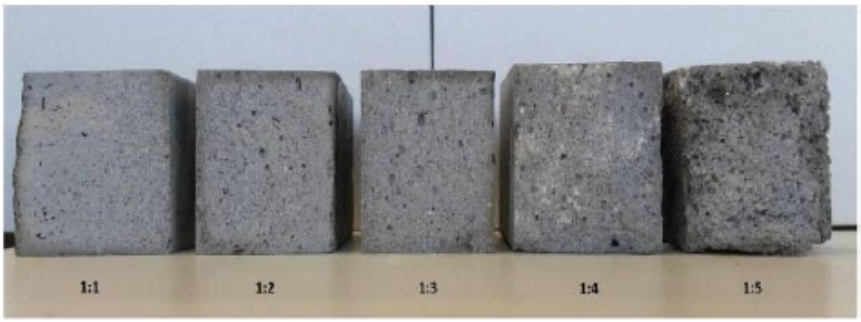

Fig. 1. Cross sections views of the produced GP-mortars.

III. RESULTS AND DISCUSSION

3.1. Step – 1: varying the ratio B/A

The consistency of the fresh GP-mortars gives an indication of the materials workability and its real possible application. The suboptimal consistency strictly depends on the intended specific application. In any case, a too pasty (< 15 cm) or, on the contrary, a too fluid (> 25 cm) slurry may generate voids within the matrix, aggregate segregation, and delay in setting and curing – with subsequent issues on matrix uniformity and on the overall performance. In this study, considering the expected application in construction, a consistency ranging between 18–22 cm guarantees a good material workability with suitable compaction and homogeneity [10]. However, it must be recalled that consistency can be modified by adding specific chemicals (i.e., plasticisers), but their use is avoided in this study to prevent any undesired effects. The mortars measured consistencies (spread) are reported in Table 1. It is observed that decreasing the L/S ratio, that is to say increasing the amount of the admixed aggregate, mortars become more pasty and, consequently, their workability decreases. As a direct consequence, larger voids are formed as shown in Figure 1. Only the specimen n. 3 (ratio B/A - 1:3) presents a suboptimal consistency (21 cm).

The bulk density of the 28 days hardened GP-mortars resulted: GP – 1307 Kg/m^3; mortar ratio 1:1 - 1440 Kg/m^3; mortar 1:2 - 1771 Kg/m3; mortar 1:3 – 1832 Kg/m^3; mortar 1:4 - 1921 Kg/m^3; mortar 1:5 - 1765 Kg/m^3. GP-binder is reported for comparison. It is observed that the bulk density increases with the relative amount of aggregates. However, the formulation n. 5 (ratio B/A - 1:5) shows an anomalous behaviour that is caused by its very poor workability, which does not allow a good compactness. That is also evident from Figure 1.

Water sorptivity was evaluated by immersion and by capillary action (coefficient of capillary). The calculated values are shown in Figure 2 A and B, respectively. The GP-binder water absorption by

immersion resulted equal to 38%. This high value is due to a large number of small pores that are present in the gel, as reported in [9]. In the GP-mortars, the porosity is filled up by the aggregate leading to smaller values. This effect is proportional to the amount of sand. In general, the reported values are suitable for applications in construction. The same observations may be reported for the capillarity absorption. Again, the value shown by the GP-binder resulted higher than the mortars' due to the number of small and interconnected pores through the binder gel. This activates the water uprising action and, hence, a higher capillarity. On the contrary, the sand of the mortars fills up the pores, then preventing the water to rise. Consequently, smaller values are observed. Again, the sample n. 5 shows an anomalous behaviour due to the presence of the large voids. According to the physical structure of the various mortars, and depending on the quantity of binder in the matrix, the coefficient C tends to diminish.

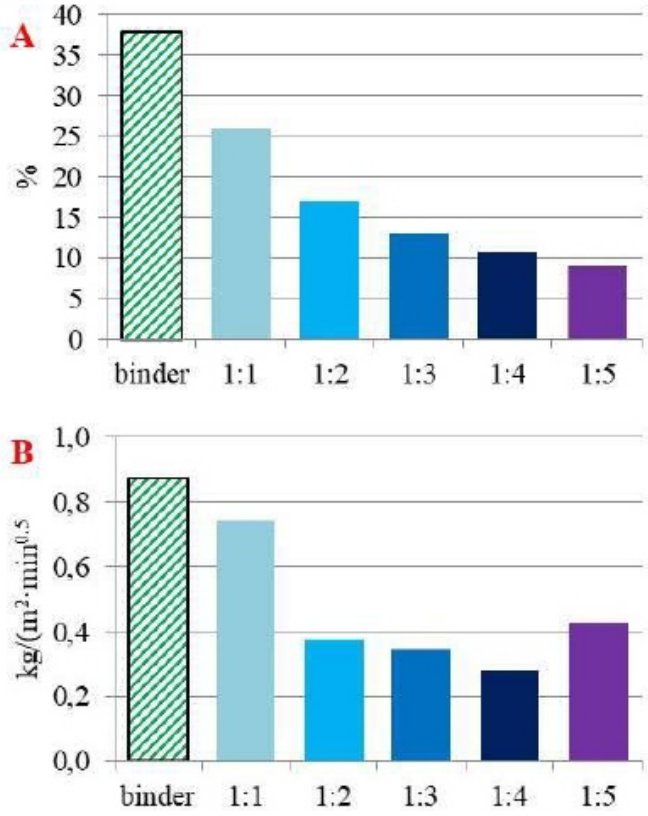

Fig. 2. Water sorptivity by immersion (A) and by capillary action – coef. of capillary (B).

Generally speaking, the mortars for masonry applications must show a compressive strength ≥ 10 MPa (class of resistance M10, or higher) in order to be suitable for structural applications in construction. For each tested formulation, uniaxial compressive strength (UCS) and bending resistance (BR) were assessed at 28 days of curing. Deflection and strain (at rupture) were also calculated.

Figure 3 shows the calculated values: BR (A), UCS (B), relative deflection (C), and strain (D). It is observed that the BR of GP-mortars ns. 2, 3, and 4 resulted higher than the one of the binder. Indeed, the addition of sand improves the resistance to deformation. Mortar n. 5 showed a value close to the binder;

the same could be observed for specimen n. 1 considering the calculated standard deviation. In detail, the calculated BR values resulted: binder - 3.05±0.37 MPa; ratio 1:1 – 2.45±0.49 MPa; ratio 1:2 – 4.69±0.33 MPa; ratio 1:3 – 4.08±0.58 MPa; ratio 1:4 – 4.03±0.52 MPa; and ratio 1:5 – 3.09±0.26 MPa. As a general trend, having reached the maximum value for the specimen n. 2, the BR tends to decrease by enhancing the aggregate amount. On the contrary, the respective deflections increase, meaning that using larger amount of aggregate makes the material more deformable and less brittle. According to the technology of construction, and for applications in civil engineering and architecture, that is not necessarily a positive factor since a high stiffness is required for all the inflexed horizontal elements, such as beams or slabs. Furthermore, deflections should be minimized for aesthetic reasons. The compressive strength (expressed as UCS) is the key factor for evaluating a possible masonry application. It is observed that all the produced GP-mortars are suitable for structural applications in construction, generally showing UCS ≥ 10 MPa. Mortar n. 3 presented the highest value. Mortars n. 1 and 2 show similar values. Here, it seems that the aggregate contribution to compression strength is small, so the overall resistance is entrusted to the binder (that is present in higher quantities). By comparing the GP-binder with mortars n. 1 and 2, a constant reduction is observed, which is caused by the decreasing content of binder in the mixes. Mortars n. 4 and 5 show a UCS drop. This is particularly evident for the highest sand content (1:5). In detail, the calculated UCS values were: binder - 22.15±1.22 MPa; ratio 1:1 – 20.77±0.91 MPa; ratio 1:2 – 20.32±0.71 MPa; ratio 1:3 – 21.66±0.03 MPa; ratio 1:4 – 17.75±0.95 MPa; and ratio 1:5 – 14.54±0.93 MPa. According to UNI-EN-998-2, formulated GP-mortars n. 1, 2, and 3 are classifiable as M20; GP-mortar n. 4 as M15; GP-mortar n. 5 as M10. Calculated strains demonstrate that the addition of sand improves the stiffness of the material. Calculated values range between 1.7% and 2.2%.

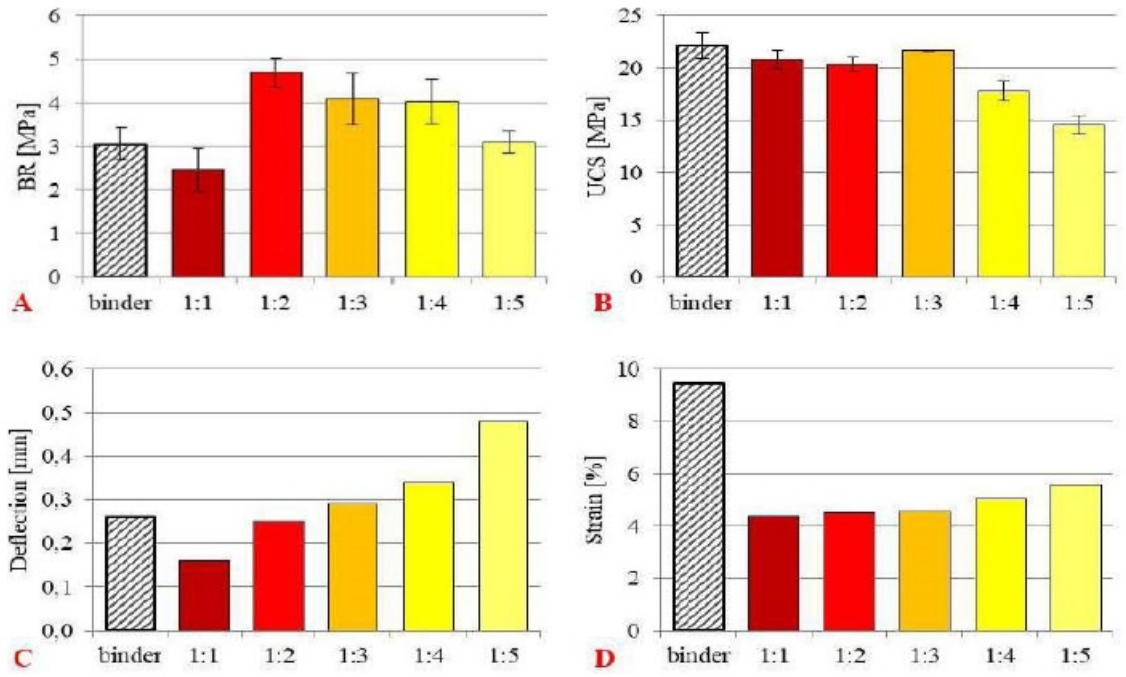

Fig.3. Mechanical performance: BR (A), UCS (B), deflection (C), and strain (D).

3.2. Step – 2: curing at various temperature

This step has been designed in order to understand which is the most effective curing temperature, and the corresponding duration. In accordance to EN 1015-11 and EN 998-2 (standards for masonry mortars) the mortars characteristic UCS was assessed at the 28th day of curing. UCS tests were also performed at the 1st and 7th days of curing in order to evaluate the progression of strengthening. Geopolymerization is a complex process that involves many chemical reactions to form a stable and uniform gel [11, 12]. These reactions usually start immediately after having mixed the alumino-silicate source (solid raw materials, in this case 70 wt.% of BFA and 30 wt.% of MK) with the alkaline activator. After the 1st day of curing, the most of the reactions have all occurred. Such reactions are highly exothermic, then a certain amount of heat is realised depending on precursors and curing conditions. According to the vast scientific literature on the topic, fresh GP are often placed at high temperature, usually 40°C or higher, to gain an early mechanical strength. That is commonly performed for a few hours up to one day.

During the previous step, the mortar n. 3 (ratio B/A - 1:3) has shown the best features for applications in construction due to its high mechanical resistance, suitable workability, and low water sorptivity. Moreover, the curing process was completely performed at ambient conditions (20 °C, 65% RH).

This specimen was then cured in distinct conditions to investigate the variabilities connected to mechanical peformance. In the first case (I) specimens were placed inside a climatic chamber where the temperature has been kept constant for the entire curing period (28 days). Temperature was set between -20°C and 100°C, with a 20°C step. This procedure envisages any possible real application (at a specific latitude / location) where a constant climatic condition occurs. Highly northern/southern hemispheres, high altitude, or desert environments are some examples. In the second case (II) specimens were placed inside the climatic chamber at constant temperature for 24 hours (one day) only. Temperature ranged from 20°C to 80°C, with a 20°C step. Afterwards, samples were cured at ambient conditions (20°C) for the other 27 days. This procedure aims at understanding if providing an initial thermal energy boosts the GP-activation granting an early/final higher resistance. Technological elements or specific applications where heat may be furnished are here envisaged.

In both the cases, the relative humidity has been kept constant at 65%, (average ambient/laboratory conditions). Results are shown in Figure 4.

Temperatures ranging 20-100°C were kept in a climatic chamber Fitoclima 300 EP10 (serie 1762) by Aralab. Lower temperatures were reached into an ordinary refrigerator equipped with temperature and humidity sensors.

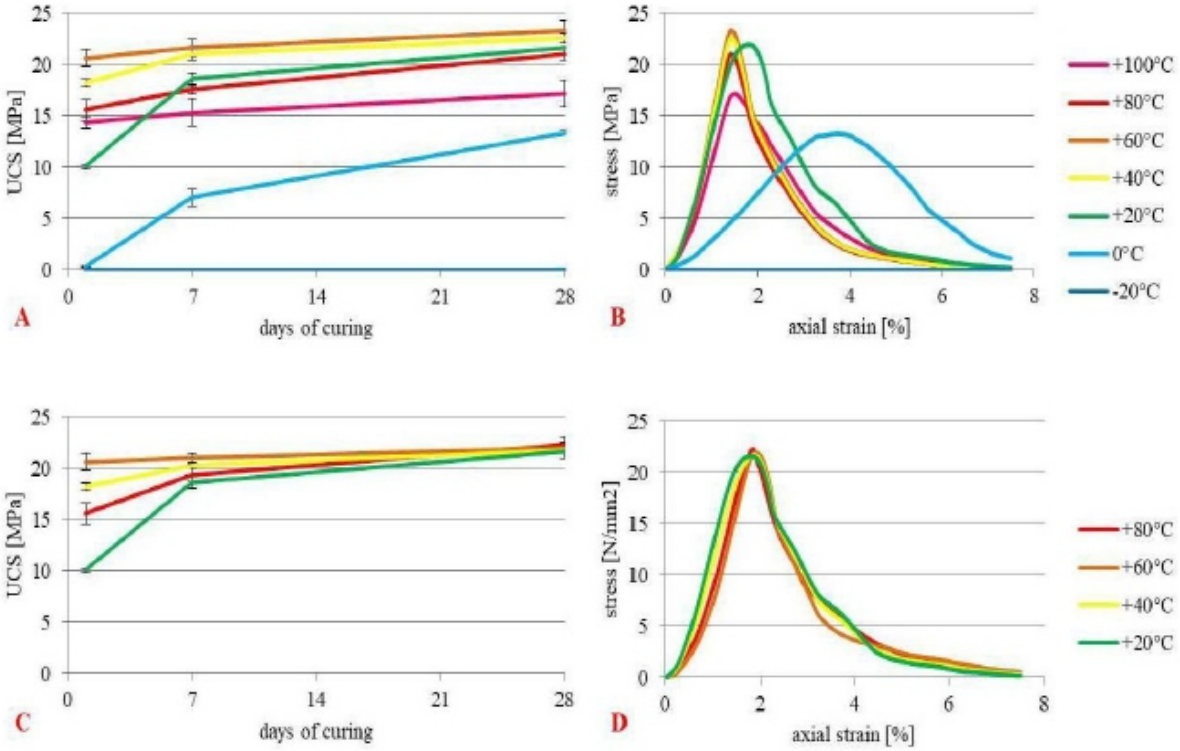

Fig.4. Mortar 1:3 mechanical performance. Curing in climatic chamber for 28 days: UCS vs. days of curing (A), stress-strain curves (B). Curing in climatic chamber for the first day only: UCS vs. days of curing (C), stress-strain curves (D).

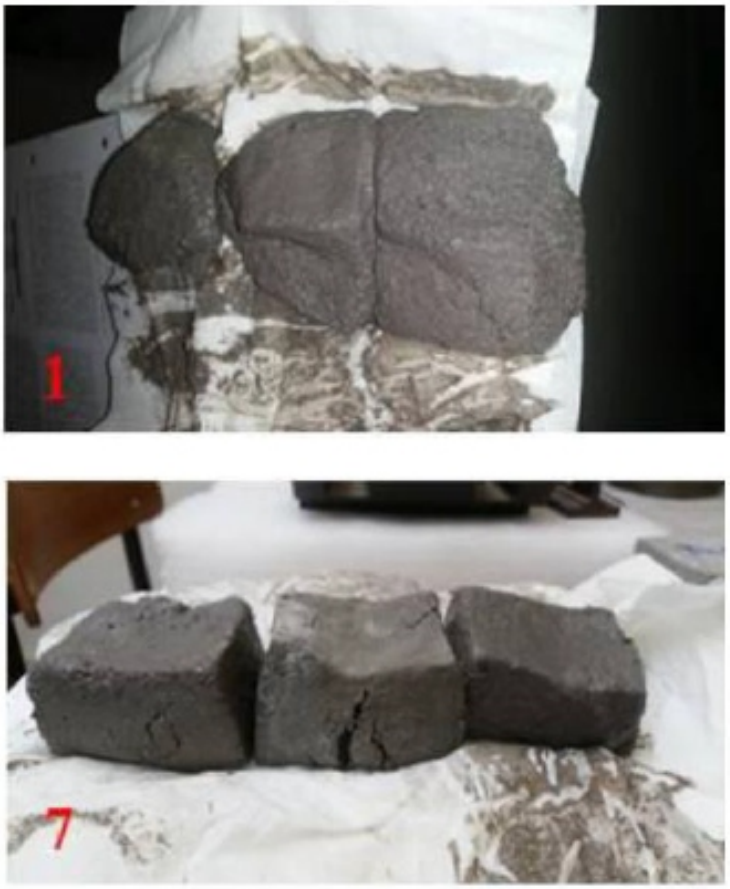

Fig.5. Specimens cured at -20°C that did not harden. From top: 1, 7, and 28 days of curing.

Figure 4 A-B and C-D shows the results of the case (I) and (II), respectively.

As a preliminary observation, for both the cases, for a temperature ranging between 20-80°C the final UCS tends to be comparable for all the specimens. That is particularly evident for the case (II). The main differences are observed at the 1st day of curing. An interesting fact is that GP-mortars cannot be cured at icy conditions (T < 0°C) (Figure 4 A) as defrosting the material, it simply melts (Figure 5). That was expectable as the immobilised (iced) water prevents the GP-reactions to occur. The immediate consequence is that the considered mortar cannot be produced and cured in extremely cold (freezing) environments. At 0°C the mortar do not show any resistance after 1 day of curing. After 7 days a moderate UCS is observed. Then, some time is needed for the material to harden and gain strength as the remaining reactions keep going on. The 28-cured sample shows a UCS equal to 13.35±0.19 MPa, making the mortar classifiable M10, then suitable for masonry applications. Increasing the temperature to 20°C, up to 60°C, the material shows an increasing early strength gain (UCS test at 1 day of curing); then the deviation diminishes resulting a final 28-day UCS > 20 MPa for the mentioned curing conditions. To summarise, the 28-day UCS values are: 20°C – 21.66±0.03 MPa; 40°C – 22.59±0.43 MPa; 60°C – 23.37±0.93 MPa. In any case, the three different (constant) temperatures lead to class M20. No beneficial effects are observed by increasing further the temperature. Indeed, at 80°C the UCS values are generally lower, with a final 28-day UCS comparable to the other curing conditions (21.04±0.53 MPa / class M20). Temperatures ≥ 100°C are detrimental for the overall performance, downgrading the material to class M15. The relative stress-strain curves at 28-days curing are shown in Figure 4 B. It is observed that increasing the curing temperature (constant for the whole curing period) the material becomes less deformable (that is also in accordance to the general curing process [9]). Anyway, the values are comparable with an average deformation of 1.5±0.17 %. On the contrary, the mortar cured at 0°C shows a strain of about 3.6%.

In the second case (Figure 4 C-D) specimens were kept into the climatic chamber for 24 hours only, where the temperature ranged from 20°C to 80°C, with a 20°C step. Subsequently, the curing process was completed (up to the 28th day) at ambient conditions (20°C). As previously discussed, the measured 1-day UCS is identical to the first test, being the specimens tested at the same stage of curing that occurred at the same conditions (Figure 4 C). It is noteworthy that only after 7 days of curing, the 20°C mortar has mainly overcome the gap with the other specimens and after 28 days of curing the measured UCS values of all the 4 specimens are almost identical. Measured values were: 20°C – 21.66±0.03 MPa; 40°C – 21.77±0.76 MPa; 60°C – 22.29±0.47 MPa; 80°C – 22.29±0.73 MPa. All the mortars resulted class M20. From the analysis of the 28-day stress-strain curves (Figure 4 D), it can also be noted that the performance of the specimens is approximately the same. This observation reveals that providing heat during the first day of curing has no influence on the final mechanical performance, in terms of both UCS and deformation.

It is important to remark that all the four tested initial curing temperatures (applied for 24 hr only) lead to a similar final UCS. Consequently, considering the energy required to heat the specimens, along with the associated pollution, it can be concluded that this material can be efficiently cured completely at room temperature. That will contribute to a cost-efficient and sustainable manufacturing. The same observation could be made comparing the overall results. Indeed, mortars cured at the various temperatures (20-80°C) are all classifiable as M20, independently of the duration of the heat application.

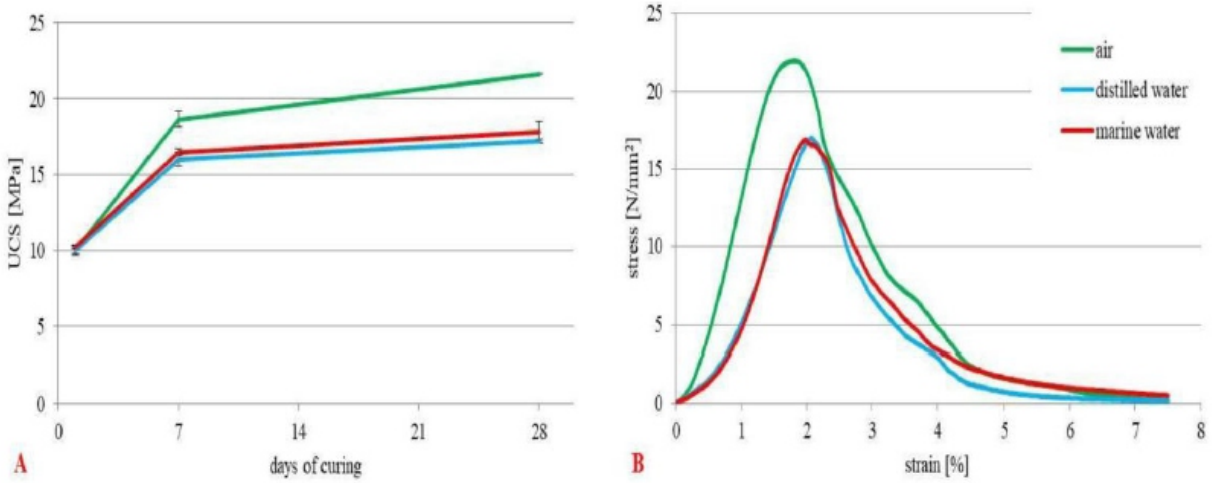

Fig.6. A: UCS values of the specimen cured in the three different means; B: stress-strain curves at 28-days of curing.

3.3. Step – 3: curing in water

This step has been designed in order to understand if the hardening and curing processes can occur submersed into water. That is aimed at investigating the possibility to use the studied GP-mortars for submersed structures and infrastructures such as bridges, piers, pipelines, etc.. Indeed, despite an

optimal architectural and structural design, frequently the material degradation may lead to a quite short service life, if adequate technological solutions are not foreseen. Then, also protective layers or coating may be considered as possible real applications.

Moreover, some particular building parts (i.e. foundations, poles, etc.) may be subjected to particular harsh situations, such as proximity to water sources or presence of clay terrain.

For this purpose, two different typologies of water have been used: distilled and salty water. The first one is aimed at testing the manufacture feasibility, the second one at simulating the salt attack of the sea. Consequently, a solution of 40‰ NaCl in distilled water was prepared. The used salinity has been selected according to the average worldwide sea salinity. The results of the UCS tests on the sample (formulation B/A = 1:3) are shown in figure 6. The mechanical behaviour of the reference mortar cured in air is shown for comparative reasons.

First of all, it must be noted that the GP-mortar hardens and cures submersed into water. Indeed, the GP is a hydraulic binder and behaves in analogy to the traditional construction materials, as the cement does. It is observed that the UCS values of the two submersed materials are equal but lower to the one of the material cured in air. Accordingly, the calculated UCS values at 28-days of submersed curing resulted: curing in air (reference) – 21.66±0.03 MPa; curing in distilled water – 17.22±013 MPa; curing in salty water - 17.80±0.71 MPa. From figure 6B it is observed that the mechanical behaviour is independent from the nature of water and that the submersed-cured GP-mortars are more deformable (~ 5.20 % strain).

3.4. Effects caused by natural ageing

In this section we will focus on the effects caused by natural aging. Understanding how the physical features might change over time, is essential to indicate a suboptimal real application. That is crucial for the mechanical performance whose evolution could prevent a novel material from particular usages or may suggest more advisable applications. Furthermore, analysing such an evolution is essential to predict durability.

Traditional mortars (whether cementitious, lime-based, or others) usually harden and cure in presence of water gaining strength over time. This natural process can last years and usually generates hydrates. Furthermore, during the hydration reaction the material can show a significant reduction in pore volume, caused by the natural evaporation of water along with its chemical consumption, and the mineralogical species transformation. Those factors usually result into a great volumetric shrinkage [13, 14]. In GP

technology, also the GP-process occurs during hardening and curing but it does not form any hydrates. Consequently, the matrix structure, along with the pore size distribution, is refined throughout the hardening process [15, 16]. That is essential to understand the evolution of the mechanical performance, or of other properties as, i.e., the water absorption.

Figure 7 shows the mechanical performance during aging. Figure 7A shows the UCS value that is observed to increase over time. Figure 7B shows the UCS improvement rate. Day 0 represents the production date; day 1 when specimens were demoulded. At this stage the material shows a break point of 10.05±0.23 MPa, already assuring the M10 classification. During the first 7 days there is a gain of 86% in CS values but then the rate slows down. At 28 days, as discussed, the break point is 21.66±0.03 MPa; at 60 days it is increased to 24.97±0.80 MPa, corresponding to a total improvement of ≈ 150%. After 120 days of curing a UCS of 27.39±1.82 MPa, with an improvement of ≈172%.

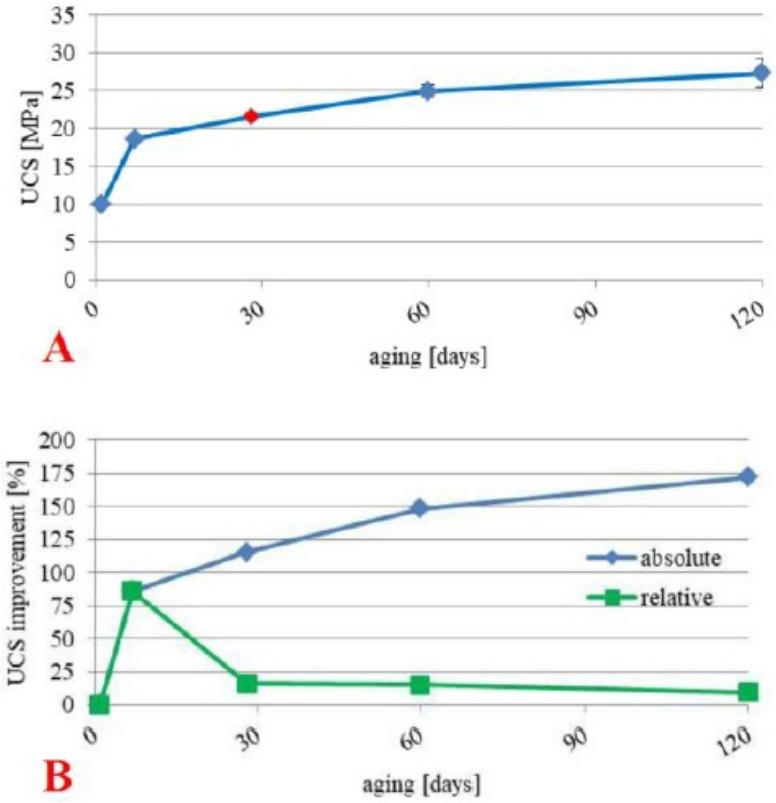

Fig.7. A: Mortar 1:3 mechanical performance. A - UCS vs. curing days (the red mark is the characteristic 28-day value); B - compressive strength improvement % (absolute and relative).

IV. CONCLUSION

This paper describes the development of GP- mortars intended for applications in construction, using BFA as binder major solid component and sand as thin aggregate. Five formulations, prepared with distinct binder/aggregate ratios, were tested. The curing temperature, duration, and medium were varied to evaluate the best conditions for a high mechanical resistance. The major conclusions are:

1. All the formulated mortars are suitable for structural applications in construction, being classifiable at least as class M10.
2. Increasing the amount of the aggregate the slurry becomes less workable, showing a decreasing consistency, the bulk density increases, and the water sorptivity, either by immersion and by capillary action, decreases.
3. The optimal binder/aggregate ratio resulted 1:3 with a 28-day bending resistance equal to 4.08±0.58 MPa, and a uniaxial compressive strength equal to 21.66±0.03 MPa (class M20).
4. An initial higher curing temperature assures high initial strength (1-day curing); however the 28-days UCS are comparable.
5. Curing the specimens at ambient conditions, without providing any external source of energy, contributes in saving electricity, lowering the manufacture costs and the CO2 emissions.
6. GP-mortar hardens submersed in water, independently of the presence of possible salts, and presents a lower UCS compared to traditional curing in air.
7. The GP-mortar keep on gaining strength during natural ageing (curing).

ACKNOWLEDGMENTS

This work is financed by Portugal 2020 through European Regional Development Fund (ERDF) in the frame of Operational Competitiveness and Internationalization Programme (POCI) in the scope of the project PROTEUS - POCI-01-0247-FEDER-017729 and in the scope of the project CICECO-Aveiro Institute of Materials, FCT Ref. UID/CTM/50011/2019, financed by national funds through the FCT/MCTES.

REFERENCE

[1] European Parliament, UE Council, UE 2008/98/CE.
[2] S.A. Kumar, "Entrepreneurship Development", New Age Int., 2008.
[3] K. Komnitsas and D. Zaharaki, "Geopolymerisation: A review and prospects for the minerals industry", Miner Eng 20, pp.1261-77, 2007.
[4] J.L. Provis and J.S.N. Van Deventer, "Alkali Activated Materials: State-of-the-Art Report", RILEM TC 224-AAM, New York: Springer, 2014, p. 32.
[5] J. Davidovits, "Synthesis of new high temperature geo-polymers for reinforced plastics/composites", Society of Plastic Engineers, Brookfield Center, pp. 151–54, 1979.
[6] M. Ghochapon, et. al., "Integration of the biorefinery concept for the development of sustainable processes for pulp and paper industry", Comp. Chem. Eng., 119, pp. 70–84, 2018.
[7] L.A.C. Tarelho, E.R. Teixeira, D.F.R. Silva, R.C.E. Modolo, J.A. Labrincha, F. Rocha, "Characteristics of distinct ash flows in a biomass thermal power plant with bubbling fluidised bed combustor", Energy, vol. 90, pp. 387-402, 2015.
[8] M. Saeli, R.M. Novais, M.P. Seabra, J.A. Labrincha, "Mix design and mechanical performance of geopolymer binder for sustainable construction and building material", IOP Conf. Series: Mater. Sci. Eng., vol. 264, id. 012002, 2017.
[9] M. Saeli et al., D.M. Tobaldi, M.P. Seabra, J.A. Labrincha, "Mix design and mechanical performance of geopolymeric binders and mortars using biomass fly ash and alkaline effluent from paper-pulp industry", Journal of Cleaner Production, vol. 208, pp. 1188-1197, 2019.
[10] R. Chudley and R. Greeno, "Building Construction Handbook"; Routledge: Abingdon, UK, 2016.

[11] P. Duxson et alt., "Geopolymer technology: The current state of the art", Journal of Material Science, vol. 42, pp. 2917–2933, 2007.

[12] K. Komnitsas and D. Zaharaki,"Geopolymerisation: A review and prospects for the minerals industry", Miner. Eng., vol. 20, pp. 1261–1277, 2007.

[13] H. Brouwers, "The work of Powers and Brownyard revisited: Part 1", Cement Concrete Res, 34 (9), pp. 1697–1716, 2004.

[14] J. Sindhunata, L. Provis, G.C. Lukey, H. Xu, and S.J.J. van Deventer, "Structural Evolution of Fly Ash Based Geopolymers in Alkaline Environments", Ind. Eng. Chem. Res., 47, pp. 2991-2999, 2008.

[15] J. Sindhunata et al., "The Effect of Curing Conditions on the Properties of Geopolymeric Materials Derived from Fly Ash", Proceedings of the International Symposium of Advances in Concrete through Science and Engineering, IL, Mar 21-24, 2004.

[16] D. Hardjito and B.V. Rangan, "Development and properties of low-calcium fly ash based geopolymer concrete", Research report GC1, Curtin University of Technology, Australia, Perth, 103 s, 2005.

ISSN Print : 2320-2092, Online : 2321-2071

Combined Steering and Acceleration Optimized Controller for an Autonomous Ground Vehicle

[1]Murad Dawood, [2]Mohamed Abdelaziz, [3]M Ghoneima, [4]S Hammad
[1]Department of Mechatronics, Ain Shams university,
[2]Department of Automotive, Ain Shams university,
[3]Department of Mechatronics, Ain Shams university,
[4]Department of Mechatronics, Ain Shams university
E-mail: [1]murad.dawood@eng.asu.edu.eg

A B S T R A C T

Autonomous driving has been a fast growing industry in the last decade mainly because of the improved processing capabilities of nowadays computers and moreover to increase the safety of transportation of passengers. Still with the current sophisticated processing tools, the computational burden of the nonlinear model predictive control (NMPC) in MIMO systems is still hindering further implementation in real time applications such as fully self-driving vehicles. We tackle this issue by developing a controller that is able to guide the vehicle through acceleration and steering to track a predefined path accurately while paying attention to the comfort of the passengers and moreover capable of running in real time. CaSAdi is used to formulate and solve the NMPC problem. MATLAB simulations show the effectiveness of the developed controller.

Keywords - Autonomous Vehicle, Model Predictive Control, Nonlinear Systems, Multiple Shooting, Path Tracking.

I. INTRODUCTION

The competition in the automotive industry has increased significantly in the last few years with many companies entering the race to achieve a fully autonomous vehicle capable of transporting passengers safely. Among the challenges facing the fully autonomous driving cars is the path tracking, where the controller has to guide the vehicle accurately on a predefined path by manipulating several control signals that comprise the steering angle, the acceleration and braking signals simultaneously. Over the years different techniques has been used ranging from kinematic and geometric methods such as: Stanley[1], pure pursuit[2], and recent hybrid methods incorporating both of them as in [3]where the control signal is the weighted sum of the two controller, to optimal control methods as in [4]where he formulated a LQ-Preview controller for lateral guidance of a vehicle, [5] used a LQR controller to guide a fast off road mobile robot, H∞ has also been used in [6]to design a lane keeping controller, and intelligent control methods as in [7]where a Neuro-fuzzy controller is developed to handle the path tracking while adapting to different road friction coefficients. Model predictive control has been tested extensively in the literature due to its ability to handle multiple constraints and account for future disturbances [8], in [9]a robust MPC controller combined with optimal preview controller was developed for path tracking, in [10] a LTV-MPC with look up tables for parameters selection were

developed for controlling the front steering of the vehicle, , [11] used NMPC with a genetic optimization solver to control the steering and velocity of an autonomous vehicle, [12]implemented fast NMPC to control for point stabilization and trajectory tracking of mobile robots, [13]used linear MPC to control the front steering of a mobile robot for the objective of path tracking and obstacle avoidance. In this paper we implement a fast NMPC for controlling the front steering and acceleration of a golf kart that would be used to transport passengers on campus. The inner model of the NMPC is a nonlinear dynamic bicycle model. The rest of the paper is arranged as follows, section 1 discusses the model used in the development of the controller, in section 2 we formulate the nonlinear model predictive controller along with the constraintsof the states, the performance of the controller based on simulations are presented in section 3, and lastly we conclude the presented work in section 4.

II. MODELLING

We represent the dynamics of the vehicle using the bicycle model[14]. The following assumptions are considered: 1) we only consider in-plane forces (Fx and Fy) while the out-of-plane forces (Fz) are neglected, 2) the vehicle is rear wheel driven with no brakes on the front wheels; hence no longitudinal force from the front tire; i.e. Ffx=0, 3) all nonlinear forces acting on the vehicle such as drag forces are neglected.

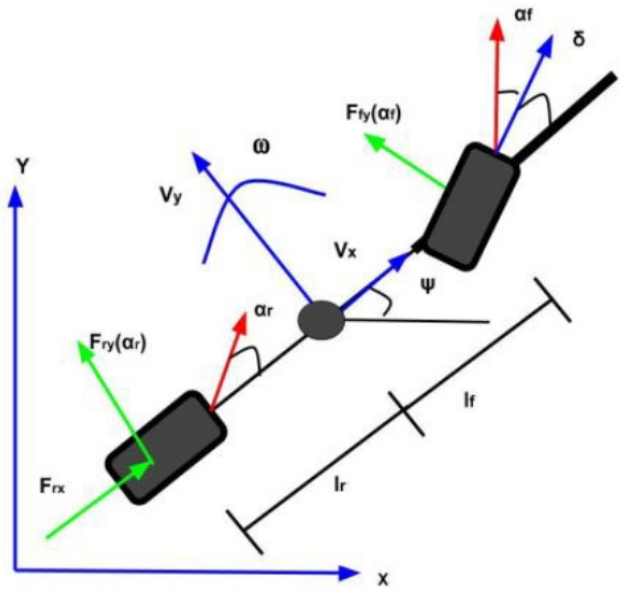

Figure 1 Dynamic Bicycle model

In Figure (1) the forces acting on the wheels along with the tires slip angles are shown. Fi,j represent the linear and longitudinal tire forces acting on the rear and front wheels subscript —i‖ ϵ {f, r} and denotes the front or rear and —j‖ ϵ {x, y} and denotes the longitudinal and lateral directions. αi is the tire slip angle of the front and rear tires.

The mathematical model can then be derived as in[15], [16]:

$$\dot{X} = \dot{x}\cos(\psi) - \dot{y}\sin(\psi)$$
$$\dot{Y} = \dot{x}\sin(\psi) - \dot{y}\cos(\psi)$$
$$\dot{\psi} = \psi$$
$$\ddot{x} = \dot{\psi}\dot{y} + a_x$$
$$\ddot{y} = \frac{1}{m}(F_{ry} + F_{fy}\cos(\beta) - m\dot{\psi}x)$$
$$\ddot{\psi} = \frac{1}{I_z}(F_{fy}\, l_f \cos(\beta) - F_{ry} l_r)$$

The lateral forces are calculated as linearized functions of the tire slip angles:

$$F_{iy} = C_i \alpha_i$$

Wherex and y are the longitudinal and lateral velocities of the C.G. in the fixed body frame, X and Y are the velocities of the C.G. in the inertial frame, and ψ being the yaw rate. The longitudinal acceleration is calculated as the summation of two parts: ψ y the centripetal acceleration and ax the acceleration resulting from the forces acting on the vehicle and will be an input to the model. The states of the derived model are X= [X Y ψx y ψ] and the inputs to the model are U= [δfax], the parameters used are in Table 1.

m	Mass of vehicle	420 kg
I_z	Yaw moment of inertia	300 kg.m^2
l_f	Distance from CG to front wheel axis	0.62 m
l_r	Distance from CG to rear wheel axis	0.58 m
C_f	Front wheel cornering stiffness	12000 N/rad
C_r	Front wheel cornering stiffness	20000 N/rad

Table 1 parameters of the golf kart

III. CONTROLLER

In this paper we apply the NMPC technique to develop a point-by-point path tracking controller, we'll nowdefine the optimal control problem, constraints and define the algorithm developed.

A. Cost function

The goal of the path tracking controller in general is to minimize the deviation from the planned path for the vehicle, and to ensure the comfort of the passengers; hence the (OCP) is formulated as follows:

$$\min_{\zeta,u} J := \sum_{i=1}^{Np} \| X(k+i \mid k) - X_{ref}(k+i \mid k) \|_Q^2 +$$

$$\sum_{i=1}^{Nc} \| \Delta u_k (k+i \mid k) \|_R^2$$

$$s.t. X_{k+1} - \phi_k (X_k, u_k) = 0,$$

$$\Delta u_k = u_{k+1} - u_k,$$

Where the first term of the function penalizes the error between the predicted state and the reference state, and the second part penalizes the rate of change of the control actions, Q and R being the weight matrices, and Φ represents the system dynamics at each time step. The OCP is then discretized using multiple shooting[17] to a NLP and solved using the IPOPT solver in CaSAdi[18] framework.

B. Constraints

For the NMPC formulated we have a set of constraints for both the inputs and the states of the system.

$$\begin{gathered} -20^\circ \qquad\qquad 20^\circ \\ -1.5m/s^2 \leq u \leq 1m/s^2, \\ -18^\circ \leq \dot{\Psi} \leq 18^\circ, \\ -4m/s^2 \leq \ddot{y} \leq 4m/s^2 \end{gathered}$$

Where the steering angle limit represents the physical limit of the steering system, and the limitations on the yaw rate and the lateral acceleration are to ensure a smooth ride since higher rates can sacrifice the passengers comfort. The algorithm implemented as follows as in 1.

Algorithm 1 point-by-point tracking
1: While current state ≠ End of path do
2: Measure the state x(n)of the system, n = 0,1,2, ...
3: Set initial state x_o = x(n)
4: Search for the nearest point in the path
5: Set the nearest point in the path as the reference state x(i), i = 1,2, ..., End of path
6: Solve the OCP over the prediction N and find minimizing control sequence $u^*(n)$
7: Apply the first element of the sequence $u^*(n)$ and discard the rest.
8: end while

IV. SIMULATIONS AND RESULTS

Since our aim is to drive the golf kart on campus, we are more concerned with the turns handling rather than high speed driving; for this we impose 2 different tests: 1) A smooth circular path2) A curvy Sin

wave path, the simulations were done on MATLAB. The options for the IPOPT solver throughout the simulations are in table 2.

Max iterations	2000
Acceptable convergence tolerance	1e-8
Stopping criterion based on objective function change	1e-6

Table 2 options for IPOPT solver

A. Smooth circular path

The reference path shown in Fig 2 is defined as:

$$X_{ref} = 50 * \cos(\omega)$$
$$Y_{ref} = 50 * \sin(\omega)$$
$$\omega = 0 : 2\pi$$

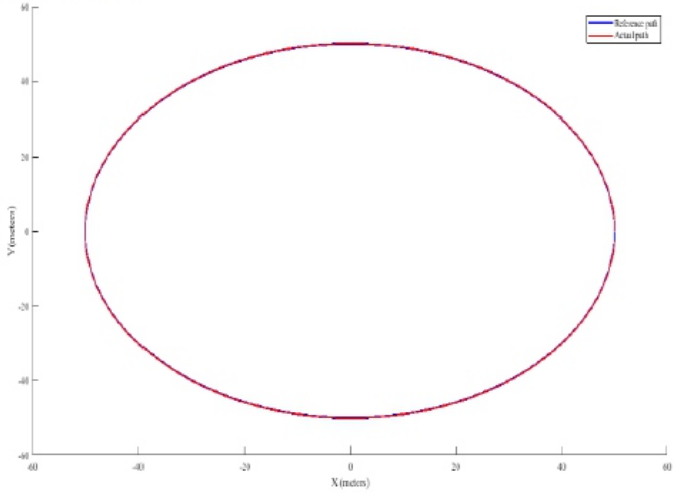

Figure 2 Reference and Actual Paths

And the weight matrices and reference velocity for the scenario are as follows: Q=[1;0;0;1;7;7], R=[20;10], where Q and R are diagonal matrices, V_{ref}= 4 m/s.

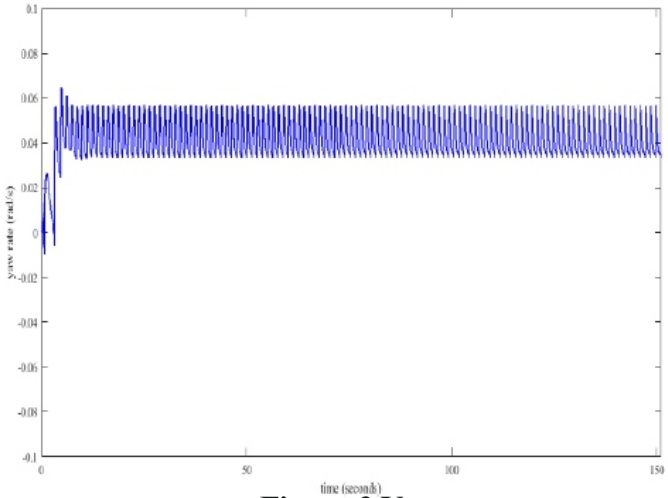

Figure 3 Yaw rate

The vehicle followed the path with an average error of 6.33 cm from the targets, figure 5. The average speed along the path was 3.7 (m/s) and reached a maximum speed of 4.1 (m/s). Figures 3 and 4 show that the yaw rate was within limits the whole path, and the yaw angles of the reference and the actual paths are almost the same. The average iteration time took 0.0484 seconds which shows the algorithm can be implemented in real time.

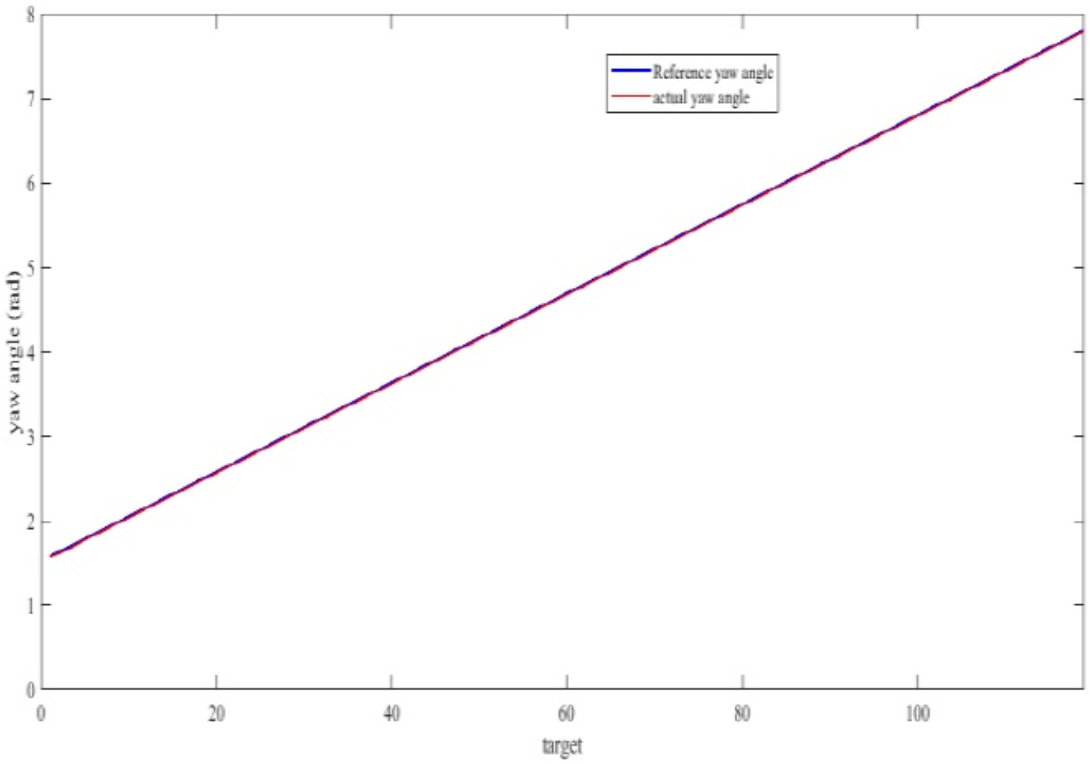

Figure 4 Reference and Actual Yaw angles

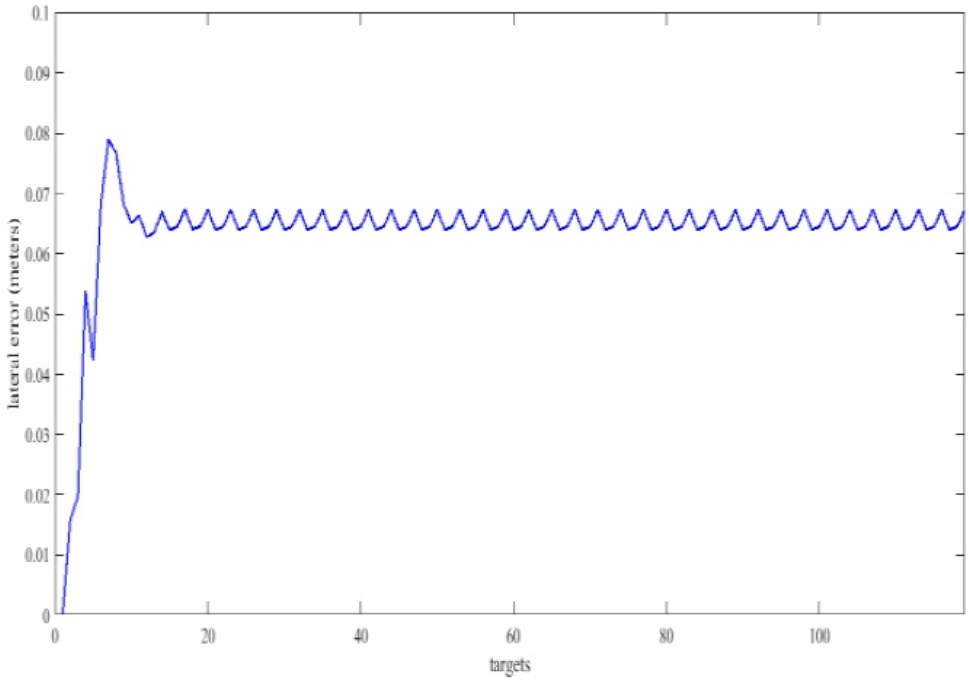

Figure 5 Offset errors along the path

B. Sin wave path

The reference path shown in Fig 6 is defined as:

$$Y_{ref} = 5 * \sin(X_{ref})$$
$$X_{ref} = 0 : 2 * \pi$$

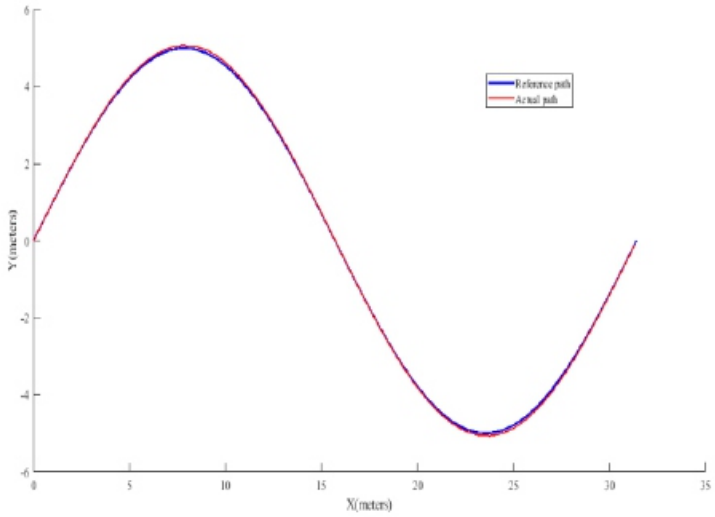

Figure 6 Reference and Actual Paths

And the weight matrices and reference velocity for the scenario are as follows: Q=[3;0;0;0.1;40;40], R=[10;10], where both Q and R are diagonal matrices, $V_{ref} = 2\frac{m}{s}$. The vehicle was able to follow the path with acceptable deviations of average 12.5 cm from the targets along the path, figure 9, with an average velocity of 1.5m/s and reached max velocity 1.9 m/s. Figure 7 show the yaw rate along the path which was within the limits the whole path, figure 8 the actual yaw angles and the reference yaw angles of the vehicle along the path. The average computation time per iteration was 0.0448s and the max iteration time was 0.2008s.

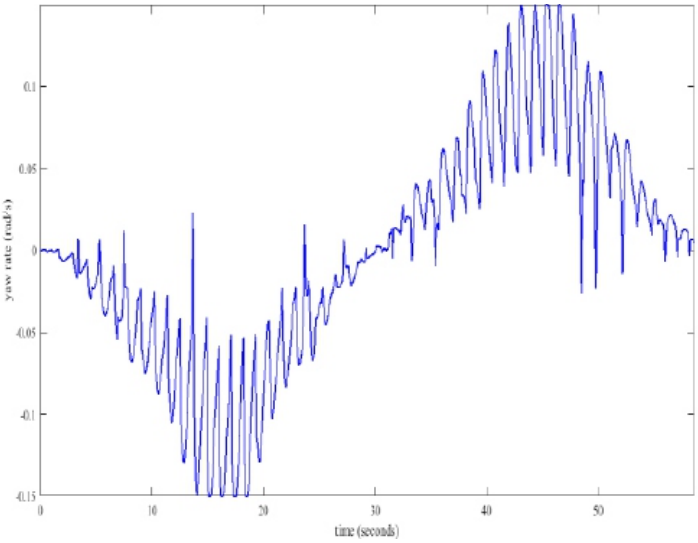

Figure 7 Yaw rate

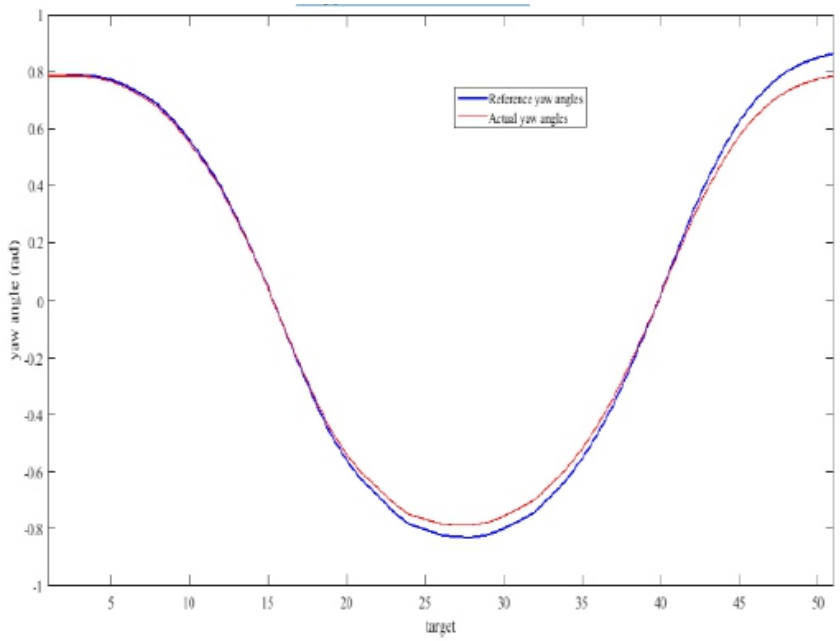

Figure 8 Reference and Actual Yaw angles

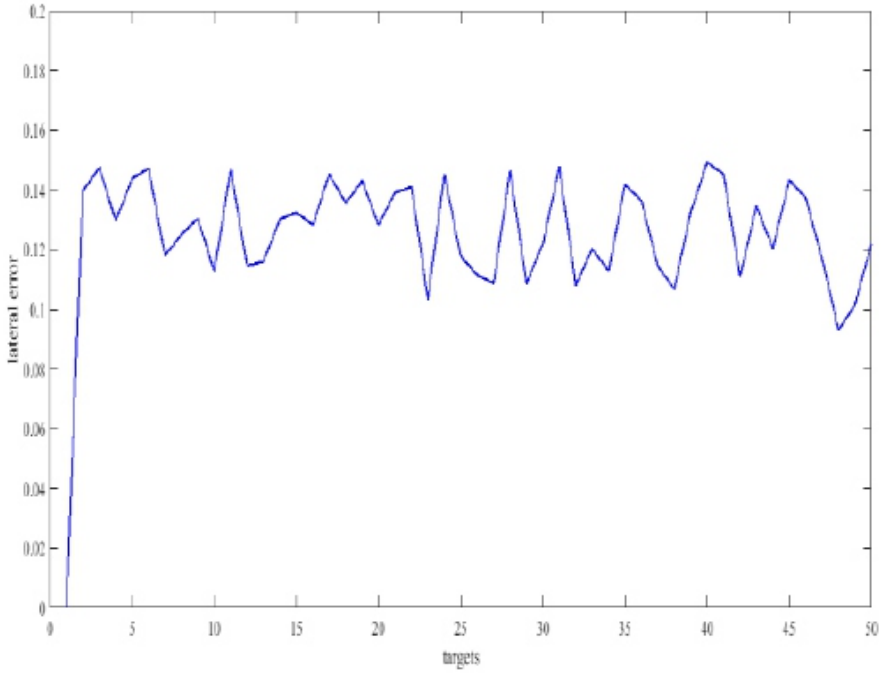

Figure 9 Offset errors along the path

V. CONCLUSION

In this paper we presented a nonlinear model predictive controller to control the front steering and acceleration of a golf kart to be driven on campus with the passenger's safety taken in consideration. An acceleration-input nonlinear bicycle model is developed and used in the control design. The OCP was formulated by setting the objective function and the limits of the states and the control signals, which was then discretized into a NLP using Multiple Shooting Method and solved with IPOPT with the aid of CaSAdi. Multiple simulations with different scenarios to test the accuracy and run time of the controller

have been run. The results show the effectiveness of the controller to follow the paths while maintaining passengers' safety and the feasibility to test the controller in real time.

REFERENCE

[1] S. Thrun et al., —Stanley: The robot that won the DARPA Grand Challenge,‖ J. Field Robot., vol. 23, no. 9, pp. 661–692, Sep. 2006.

[2] R. C. Coulter, —Implementation of the Pure Pursuit Path Tracking Algorithm,‖ p. 13.

[3] Á. Domina and V. Tihanyi, —COMBINED PATH FOLLOWING CONTROLLER FOR AUTONOMOUS VEHICLES,‖ no. 2, p. 8, 2019.

[4] L. Saleh, P. Chevrel, and J.-F. Lafay, —Optimal Control with Preview for Lateral Steering of a Passenger Car: Design and Test on a Driving Simulator,‖ in Time Delay Systems: Methods, Applications and New Trends, vol. 423, R. Sipahi, T. Vyhlídal, S.-I. Niculescu, and P. Pepe, Eds. Berlin, Heidelberg: Springer Berlin Heidelberg, 2012, pp. 173–185.

[5] M. Fnadi, B. Menkouz, F. Plumet, and F. Ben Amar, —Path Tracking Control for a Double Steering Off-Road Mobile Robot,‖ in ROMANSY 22 – Robot Design, Dynamics and Control, vol. 584, V. Arakelian and P. Wenger, Eds. Cham: Springer International Publishing, 2019, pp. 441–449.

[6] F. Roselli et al., —H∞ control with look-ahead for lane keeping in autonomous vehicles,‖ in 2017 IEEE Conference on Control Technology and Applications (CCTA), Mauna Lani Resort, HI, USA, 2017, pp. 2220–2225.

[7] B. Aalizadeh, —A neurofuzzy controller for active front steering system of vehicle under road friction uncertainties,‖ Trans. Inst. Meas. Control, vol. 41, no. 4, pp. 1057–1067, Feb. 2019.

[8] C. E. García, D. M. Prett, and M. Morari, —Model predictive control: Theory and practice—A survey,‖ Automatica, vol. 25, no. 3, pp. 335–348, May 1989.

[9] Yu, J., Guo, X., Pei, X., Chen, Z. et al., —Robust Model Predictive Control for Path Tracking of Autonomous Vehicle,‖ SAE Technical Paper 2019-01-0693, 2019.

[10] Wang, Zejiang & Bai, Yunhao & Wang, Junmin & Wang, Xiaorui, "Vehicle Path Tracking LTV-MPC Controller Parameter Selection Considering CPU Computational Load" ,Journal of Dynamic Systems, Measurement, and Control 141, 2018.

[11] X. Du, K. K. K. Htet and K. K. Tan, "Development of a Genetic-Algorithm-Based Nonlinear Model Predictive Control Scheme on Velocity and Steering of Autonomous Vehicles," in IEEE Transactions on Industrial Electronics, vol. 63, no. 11, pp. 6970-6977, Nov. 2016.

[12] M. W. Mehrez, G. K. I. Mann, and R. G. Gosine, —Stabilizing NMPC of wheeled mobile robots using open-source real-time software,‖ in 2013 16th International Conference on Advanced Robotics (ICAR), Montevideo, Uruguay, 2013, pp. 1–6.

[13] A. Hatem, —Model Predictive Control for path tracking and obstacle avoidance of autonomous vehicle,‖ p. 13.

[14] R. Rajamani, Vehicle Dynamics and Control. Boston, MA: Rajesh Rajamani, 2012.

[15] Fabio Faliero, "NMPC Design For Autonomous Driving Applications", Master's thesis,2018

[16] A. Liniger, J. Lygeros, M. Morari, and E. Frazzoli, —Path Planning and Control for Autonomous Racing,‖ 2018.

[17] Moritz Diehl, Hans Georg Bock, Holger Diedam, Pierre-Brice Wieber, "Fast Direct Multiple Shooting Algorithms for Optimal Robot Control", Fast Motions in Biomechanics and Robotics, 2005.

[18] J. A. E. Andersson, J. Gillis, G. Horn, J. B. Rawlings, and M. Diehl, —CasADi: a software framework for nonlinear optimization and optimal control,‖ Math. Program.Comput., vol. 11, no. 1, pp. 1–36, Mar. 2019.

ISSN Print : 2320-2092, Online : 2321-2071

Effect of the Contraction Ratio on the Pressure Drop of MHD Flow in A Sudden Contraction

[1] Xuejiaoxiao, [2] Xiaowenfan, [3] Chang Nyungkim

[1,2]Department of Mechanical Engineering, Graduate School, Kyung Hee University, Yong-in, Kyunggi-do, 446-701, Korea,

[3]Department of Mechanical Engineering, College of Engineering, Kyung Hee University, Yong-in, Kyunggi-do, 446-701, Korea

E-mail: [1]xiaoxuejiao0128@163.com, [2]fanxiaow@163.com, [3]cnkim@khu.ac.kr

A B S T R A C T

In this study, a three-dimensional liquid metal (LM) magneto hydrodynamic (MHD) flow in a rectangular, electrically-conducting duct with sudden contraction under a uniform magnetic field is numerically examined. In spite of numerous analytic, experimental and numerical studies on MHD duct flows, detailed flow characteristics of LMMHD flows in rectangular ducts with sudden contraction of cross-section are not reported much. In the current study, detailed information on the flow velocity, pressure, Lorentz force, current and electric potential of the MHD duct flow is investigated with the use of commercial software CFX. Features of the MHD duct flow with sudden contraction under a uniform magnetic field are discussed in view of the interdependency of the flow variables involved. Besides, cases with different contraction ratios for sudden contraction are considered to investigate the geometrical effect on the pressure drop. The results show that with the increasing of the contraction ratio, the total pressure drop decreases.

Keywords - Liquid Metal, MHD, numerical Analysis, Sudden Contraction.

I. INTRODUCTION

Magneto-hydrodynamic (MHD) flows play a crucial role in the field of liquid metal fusion blankets. The liquid metal breeding blanket is one of the key components for power extraction, tritium breeding, and radiation shielding in fusion reactors [1]. DCLL (Dual-Coolant Lead-Lithium) [2], HCLL (Helium-Cooled Lead-Lithium) [3], and self-cooled lithium/vanadium [4] blankets are typical examples of liquid-breeder blankets. The pure lithium (Li) or the eutectic lead-lithium alloy (PbLi) LM is considered as coolant and as breeder material because of its high heat removal and adequate tritium breeding ratio [5]. However, for all fusion LM blanket components, magneto-hydrodynamic (MHD) effects, which is caused by the interactions of electrically-conducting-LM flow and a strong magnetic field used to confine plasma particles, will dominate the pressure drop, flow distributions and velocity profiles [6]. In fact, MHD effects and heat/mass transfer considerations are primary drivers of any LM blanket design.

For the last several decades, experimental investigations and mathematical studies for LM blankets have been performed with some limitation, since experimental works require large-size facilities and mathematical studies may not solve fully three-dimensional flow characteristics well, Nowadays, numerical methods based on computational fluid dynamics (CFD) for three dimensional MHD flowshave been widely performed with various codes developed by different research groups [7 - 10].

Tassone et al. [7] numerically studied a MHD flow around an electrically insulated heating cylinder and bounded by walls of locally different electrical conductivity under inclined magnetic field. Ni et al. [8, 9] performed numerical analyses of LMMHD flows on a rectangular collocated grid system and on an arbitrary collocated mesh, respectively, with a good accuracy. Zhou et al. [10] developed a code named MTC that can simulate 3D MHD flow in rectangular ducts, and the results matched well with Hunt's and Shercliff's analytical solutions. These codes usually need to be modified to meet specifications of a particular problem.

Lately, three-dimensional numerical works with the use of CFX code have been reported by the following researchers. Mistrangelo and Buhler [11] obtained the electric flow coupling in HCLL blanket concept in their numerical analysis, focusing on the description of velocity and current distribution in breeder units. Kim et al. [12] performed a code validation for CFX in a Test Blanket Module, and reported that CFX can predict the pressure drop well. Xiao and Kim [13] examined three-dimensional liquid–metal magnetohydrodynamic flows in a hairpin-shaped electrically-conducting duct, and found that the axial velocity in the side layer near the partitioning wall is higher than that near the outer walls.

In spite of numerous analytic, experimental and numerical studies on MHD duct flows, detailed flow characteristics of LMMHD flows in rectangular ducts with sudden contraction of cross-section are not reported much. The goal of the current study is to gain an insight into the geometrical effect of the contraction ratio on the pressure drop and on the flow distribution in the contraction segment by utilizing CFX code.

II. NUMERICAL CALCULATIONS

A. Calculation Domains

The duct geometry considered in the study is given in Fig. 1, where the width of the fluid domain is fixed to be 100 mm (the sides perpendicular to the magnetic field), while the ratio of the height of the fluid domain in the contracted duct (the sides parallel to the magnetic field) to that in the un-contracted duct is so called contraction ratio, with the expression of H2/H1. The lengths of the un-contracted and contracted ducts are 0.6 m, which is long enough for fully developed condition to be obtained before reaching the contraction and exit. The thickness of the duct walls is 5 mm. In the present study, three cases with contraction ratios 0.5 (for Case 1), 0.65 (for Case 2) and 0.8 (for Case 3) for sudden contraction are numerically investigated.

A uniform magnetic field B_0 = 0.9632 T is applied in the y direction, yielding the Hartmann number 1,000. The properties of the channel wall and working fluid are given in Table 1.

B. Governing Equations

The governing equations for a steady-state, incompressible, laminar flow of an electrically-conducting fluid under a magnetic field include the conservation of momentum, mass, charge and the Ohm's law.

$$\vec{\nabla} \cdot \vec{u} = 0 (1)$$
$$\rho \vec{u} \cdot \vec{\nabla} \vec{u} = -\vec{\nabla} p + \vec{J} \times \vec{B} + \mu \vec{\nabla}^2 \vec{u} (2)$$
$$\vec{\nabla} \cdot \vec{J} = 0 (3)$$
$$\vec{J} = \sigma \left[-\vec{\nabla} \phi + \vec{u} \times \vec{B} \right] (4)$$

where $\vec{u}$, ρ, p, $\vec{J}$, $\vec{B}$, μ, σ and ϕ are the velocity vector, fluid density, pressure, current density vector, magnetic field intensity vector, dynamic viscosity, electric conductivity and electric potential, respectively.

Substitution of the Ohm's law into the equation of charge conservation gives the Poisson's equation for electric potential

$$\vec{\nabla}^2 \phi = \vec{\nabla} \cdot \left(\vec{u} \times \vec{B} \right) (5)$$

Therefore, Equations (1) and (2) can be solved together with Equation (5) for the variables of the pressure, velocity and electric potential in the fluid domain, while $\vec{\nabla}^2 \phi = 0$; valid for the electric potential (with zero fluid velocity) in the solid domain.

C. Boundary Conditions

In the present study, the outer surface of the flow conduit is electrically insulated from the outside. No-slip condition is applied at the fluid-solid interface. At the inlet the velocity is given to be 0.008m/s, yielding the Reynolds number 2553, while at the outlet the pressure is described to be zero Pa. The whole system including the fluid and channel walls is electrically insulated from the outside, which can be written as

$$\partial \phi / \partial n = 0 (6)$$

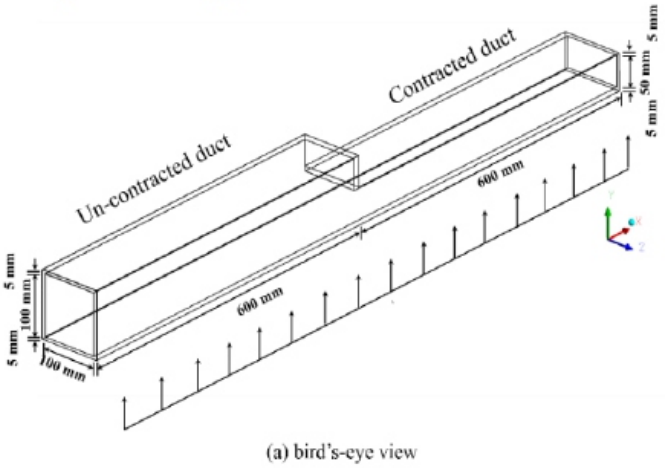

(a) bird's-eye view

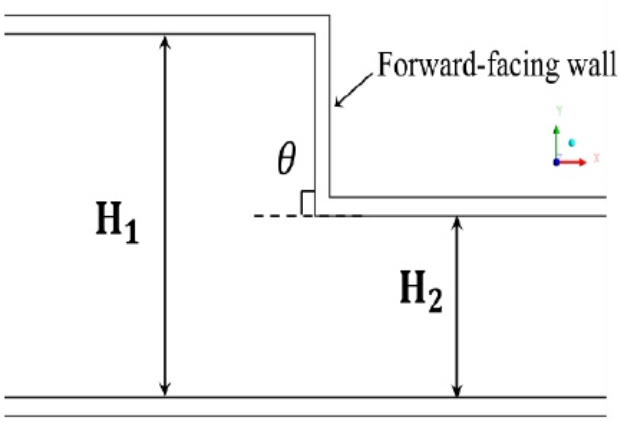

(b) side view

Fig. 1 Geometry of the duct

	density (kg/m^3)	dynamic viscosity (kg/ms)	electric conductivity (S/m)
duct wall			10^7
liquid metal	9500	1.786×10^{-3}	7.7×10^5

Table I Properties

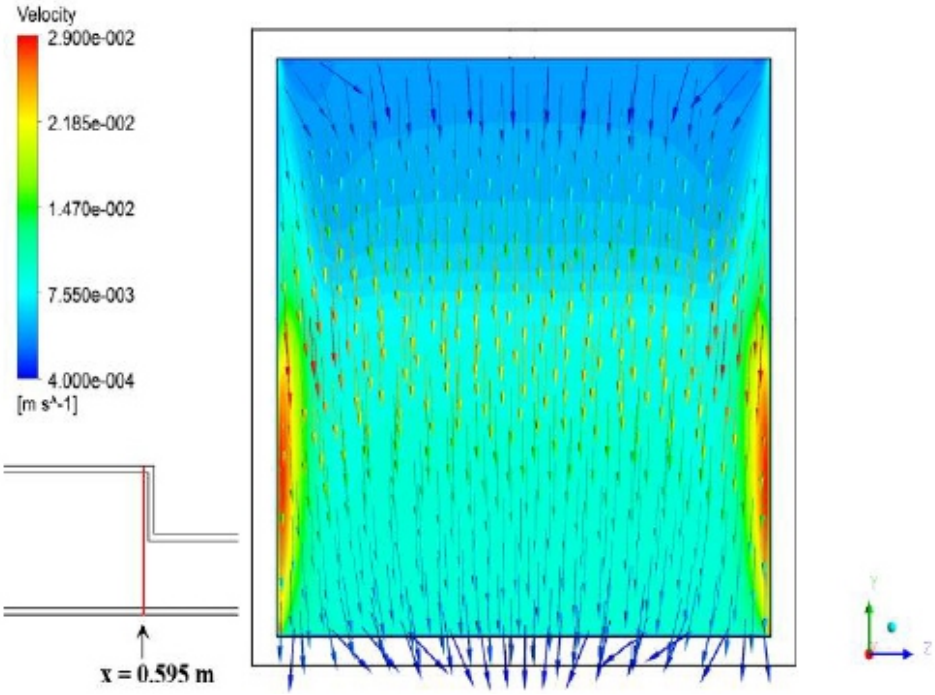

Fig. 2 Axial velocity (contour) and plane velocity (vector)in the y-z plane at x = 0.595 m in Case 1

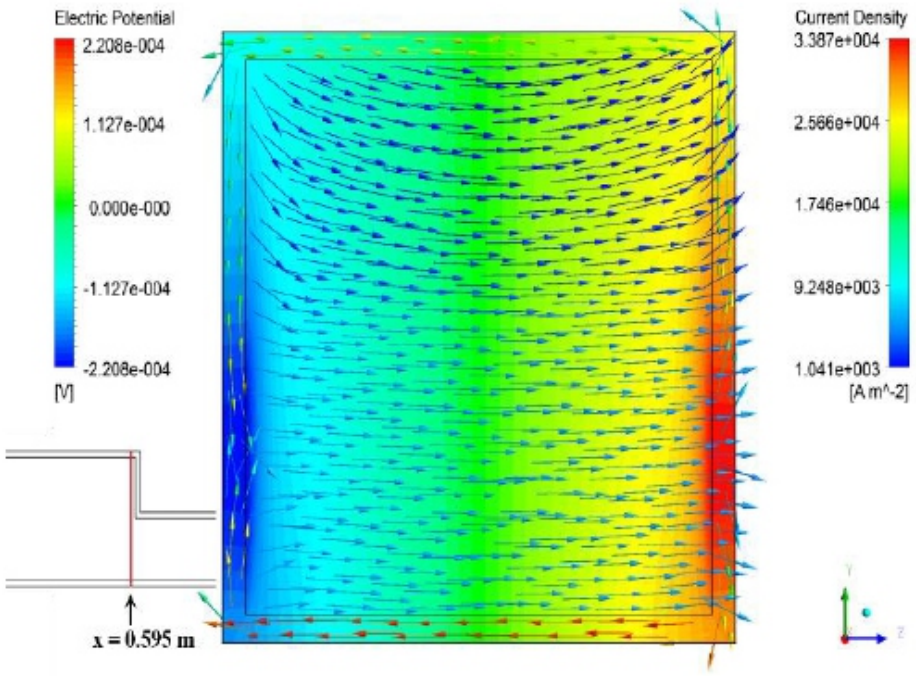

Fig. 3 Electric potential (contour) and plane current density (vector)in the y-z plane at x = 0.595 m in Case 1

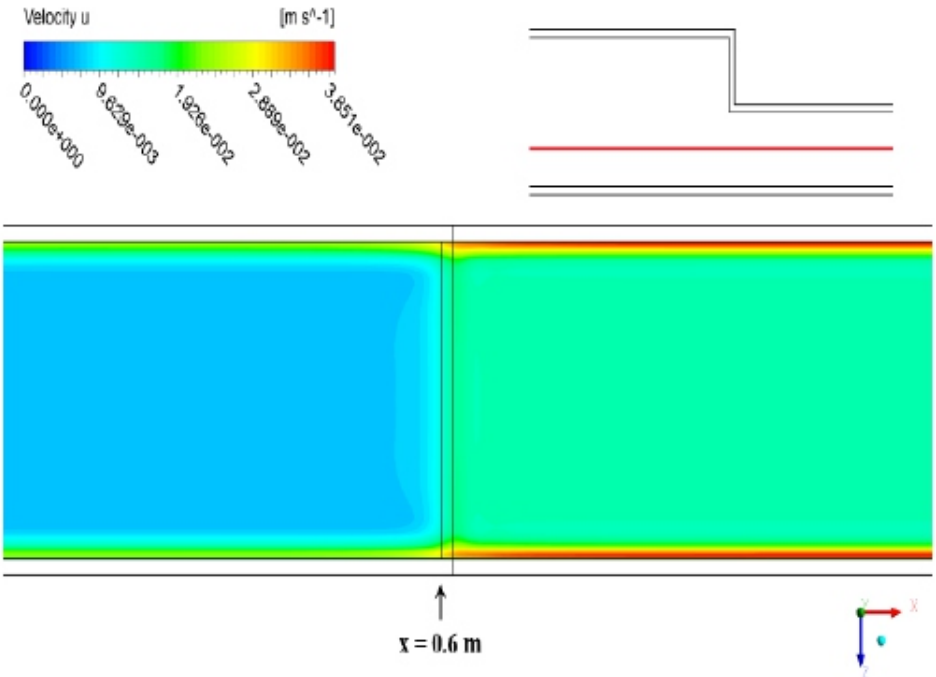

Fig.4Axial velocityin the x-z plane at y = -0.025 min Case 1

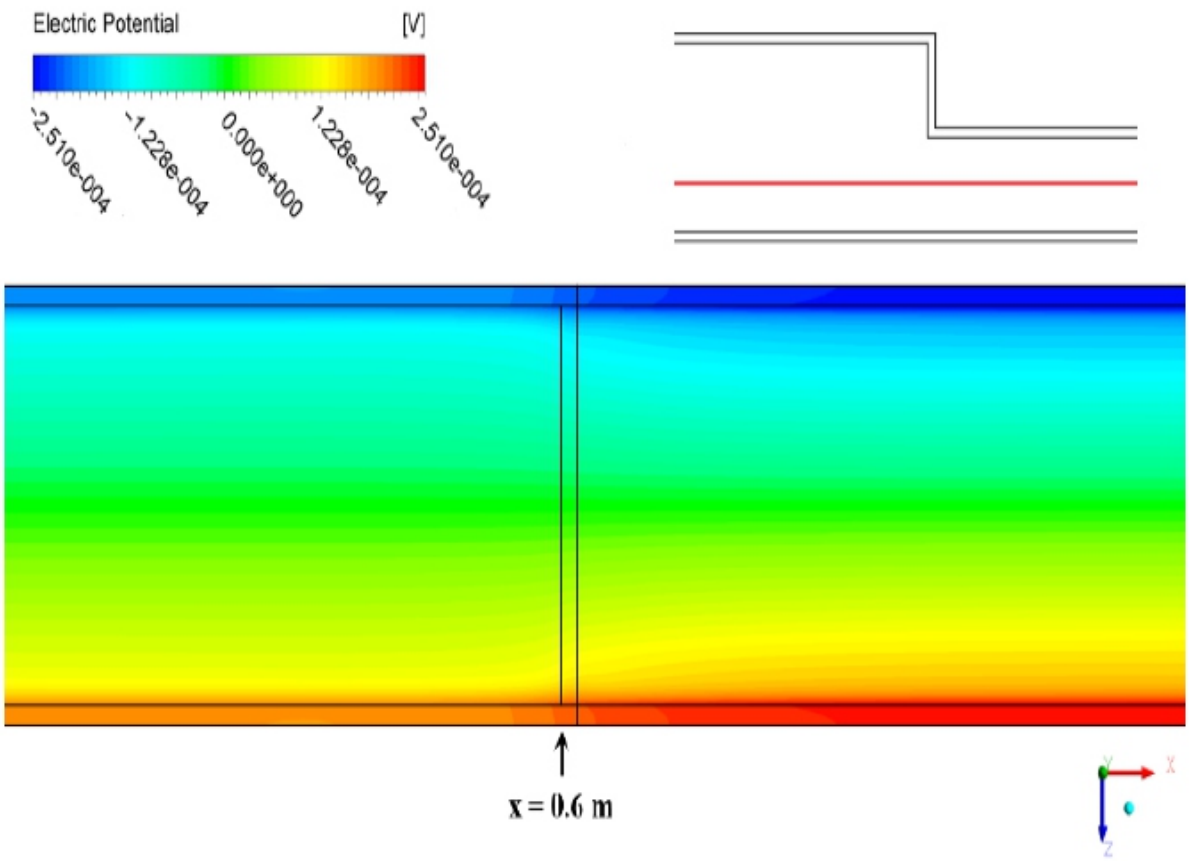

Fig. 5 Electric potentialin the x-z plane at y = -0.025 m in Case 1

III. RESULTS AND DISCUSSION

In the y-z plane at x=0.595m (located right before the contraction)the axial velocity in the upper part of the cross-section (i. e., right in front of the forward-facing wall) is quite low, while that in the lower part of the cross-section is higher with the highest velocities observed in two side layers, as shown in Fig. 2. The plane velocity in the negative y-direction is notable in the middle of the cross-section (i. e., near the leading edge of the contracted duct), which is due to the geometry of the contraction.

The plane current density and the electric potential in the same plane is shown in Fig. 3. The plane current moves rightward with relatively higher density in the lower part of the cross-section in associated with the higher axial velocity herein. The highest electric potential is obtained in fluid regionnear the lower part of the right vertical wall, while the lowest electric potential is seen in fluid regionnear the lower part of the left vertical wall.

Figs.4and 5 display the plane velocity and electric potential in the x-z plane at y = -0.025 m. Because of the contraction the average velocity in the contracted duct part is higher than that in the un-contracted duct part (Fig. 4). Also, the peak velocities in the side layers in the contracted duct part is higher than

those in the un-contracted duct part. As the fluid gets into the contracted part, the value of the induced electric potential increases, and the area of higher electric potential becomes larger in fluid region near the right side wall (i.e., near the lower wall in Fig. 5).

In a region far from the contraction, the current inside the right vertical wall of the un-contracted duct moves upward in the upper part of the right wall and downward in the lower part of the right wall, with only vertical component, respectively. While in a region near the contraction, the current inside the right vertical wall of the un-contracted duct moves upward and downward obliquely with an axial component of the current (see Fig. 6), and a portion of the above-mentioned current passes through the forward-facing wall to reach the left vertical wall. As can be seen in Fig. 7, the forward-facing wall (where the current mostly moves in the negative z direction) serves as a medium for the returning path of the current induced in the fluid region.

Figure 8 displays the axial pressure distributions in the three cases. In general, the axial pressure gradient (absolute value) in each case is higher in the contracted duct part because of higher z-directional current in association with the higher axial velocity therein. The axial pressure gradient in the un-contracted duct part in each case is almost the same from each other, while that is much different in the contracted duct part due to the different axial velocity in the contracted duct in each case. With the increasing of the contraction ratio, the pressure drop decreases significantly.

IV. CONCLUSION

In this study, numerically examined are three-dimensional liquid metal (LM) magneto-hydrodynamic (MHD) flows in a duct with sudden contraction under a uniform magnetic field applied parallel to the direction of the contraction. Here, detailed features of the LMMHD flow are examined in term of the velocity, current flow, electric potential and pressure distribution. Cases with various contraction ratios are considered. Then numerical results showed that the pressure drop is significantly influenced by the contraction ratio: with the increasing of the contraction ratio, the total pressure drop decreases. The present work can be used as the guidance of modification or optimization of the contraction pipes in liquid metal blankets.

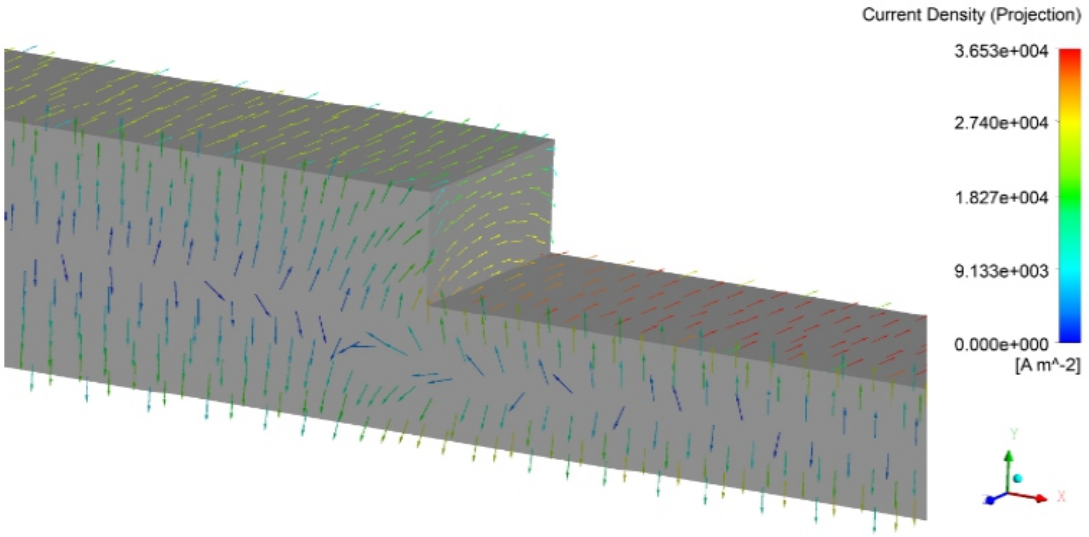

Fig.6 Current flow inside the wall near the contraction

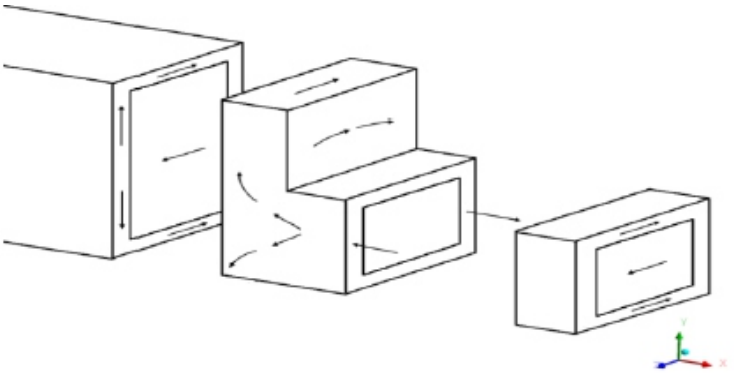

Fig.7Schematic of the current flow in region near the contraction

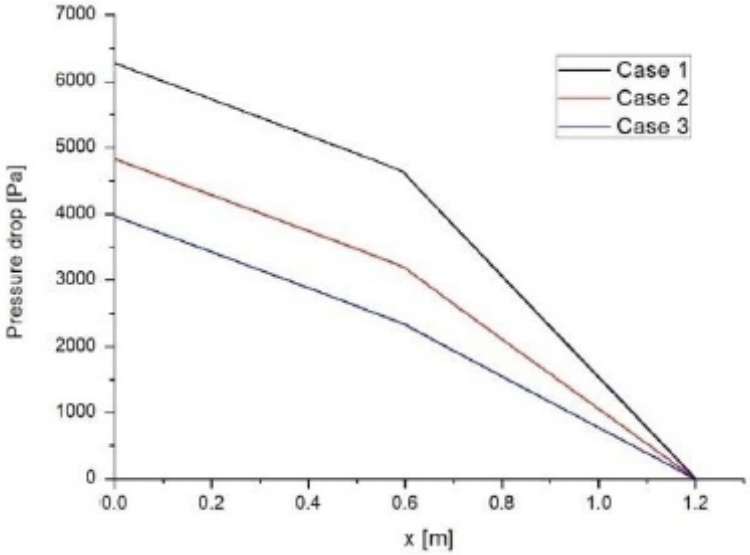

Fig.8Axial pressure distributions

REFERENCE

[1] M. Abdou, N.B. Morley, S. Smolentsev, A. Ying, S. Malang, A. Rowcliffe and M. Ulrickson, Review of blanket designs for advanced fusion reactors, Fusion Engineering and Design, vol.100,pp.2–43, 2015.

[2] S. Malang, E. Bojarsk, ualcoolant liquid metal breeder blanket, in: Proceedings of the 17th Symposiumon Fusion Technology, Rome, Italy, vol.14–18pp.1424–1428, September 1992.

[3] G. Rampal, A. Li Puma, Y. Poitevin, E. Rigal, J. Szczepanski and C. Boudot, HCLL TBMfor ITER-design studies, Fusion Engineering and Design, vol.75–79,pp.917–922, 2005.

[4] D.L. Smith, C.C. Baker, D.K. Sze, G.D. Morgan, M.A. Abdou, S.J. Piet, K.R. Schultz, R.W. Moir and J.D. Gordon,Overview of the blanket comparison and selection study, Fusion Technology, vol.8, pp. 10–113, 1985.

[5] S. Malang, P. Leroy, G.P. Casini, R.F. Mattas and Y. Strebkov, Crucial issues on liquid metal blanket design ,Fusion Engineering and Design, vol.16, pp.95–109, 1991.

[6] R. Moreau, Magnetohydrodynamics, Kluwer, 1990.

[7] A. Tassone, M. Nobili and G. Caruso, Numerical study of the MHD flow around a bounded heating cylinder: Heat transfer and pressure drops, International Communications in Heat and Mass Transfer,vol.91,pp.165-175, 2018.

[8] M.N. Ni, R. Munipalli, N.B. Morley, P. Huang, and M. Abdou, A current density conservation scheme for incompressible MHD lows at a low magnetic Reynolds number Part I: On a rectangular collocated mesh, Journal of Computational Physics, vol. 227, pp. 174-204, 2007.

[9] M.N. Ni, R. Munipalli, P. Huang, N. Morley, and M. Abdou, A current density conservation scheme for incompressible MHD lows at a low magnetic Reynolds number Part II: On an arbitrary collocated mesh, Journal of Computational Physics, vol. 227, pp. 205-228,2007.

[10] T. Zhou, Z. Yang. M.J. Ni and H. Chen, Code development and validation for analyzing liquid metal MHD flow in rectangular ducts, Fusion Engineering and Design, 85 (2010) 1736-1741.

[11] C. Mistrangelo and L. Buhler, Electric flow coupling in the HCLL blanket concept, Fusion Engineering and Design, vol.83, pp.1232-1237, 2008.

[12] S. H. Kim, M. H. Kim, D. W. Lee and C. Choi, Code validation and development for MHD analysis of liquid metal flow in Korean TBM, Fusion Engineering and Design, 87, 951-955 (2012)

[13] X. Xiao, C.N. Kim, Magnetohydrodynamic flows in a hairpin duct under a magnetic field applied perpendicular to the plane of flow [J]. Applied Mathematics and Computation, vol.240,pp.1-15, 2014.

ISSN Print : 2320-2092, Online : 2321-2071

Energy Analysis and Sustainable Operation of A Water Purification Processing Plant

[1] Idehai O. Ohijeagbon, [2] John A. Olorunmaiye, [3] Olumuyiwa A. Lasode, [4] Samuel O. Omole, [5] Mayowa A. Alonge

Mechanical Engineering Department, University of Ilorin, Ilorin, Nigeria

E-mail: [1]idehaiohi@yahoo.com, [2]adeolorunmaiye@gmail.com, [3]oalasode@yahoo.com, [4]Omolesamuel.dufil@gmail.com, [5]longhite00@gmail.com

A B S T R A C T

A water purification processing plant which employs a reverse osmosis technology was investigated in order to determine means to efficiently utilize energy in the provision of portable drinking water. The operational parameters of the operating units of the plant such as the rated power, operating efficiency and temperature were used to conduct the energy performance analysis of the plant. Also, the horsepower of the electrical generator employed as a power supplement and the average annual operating hours were used for the greenhouse gas (GHG) emission and carbon dioxide equivalents (CO2e) analysis. The average operating hours of the electrical generator is 1092 hr/yr. The overall input and output energy of the plant as well as the plant energy efficiency were determined as 200.39 and 165.08 MJ, and 82.38% respectively. The greenhouse gas (GHG) emission and carbon dioxide equivalents (CO2e) of the generating set reduces from 115.258 to 14.407 tons/yr as the horsepower of the generator reduced from 110 kVA (184.32 hp) to 13.75 kVA (23.04 hp) accordingly. Employing solar energy for powering the pumps operation instead of conventional electricity and generators helps in mitigating the use of fossil fuel generator, and lessen operational cost, air pollution and emissions respectively.

Keywords - Water purification, Energy efficiency, Solar energy, Emissions

I. INTRODUCTION

Privately owned water processing plants are on a steady rise in the world. Aside from multinational corporations playing a key role in fresh water supply chain, global trade agreements and international development organizations, such as the International Monetary Fund (IMF) and the World Bank are increasingly promoting the privatization of fresh water supplies [1]. Inadequate access to fresh clean water continues to be a source of concern in many developing countries, both in the rural and urban areas. Reasons for this predicament are inadequate social infrastructure, such as electricity and water processing plants and accompanying water supply piping-network facilities. This persistent situation has led to thriving privately owned small and medium scale water processing plants in cities across developing countries in Sub-Saharan Africa. Some of the newly commissioned commercial water processing plants are beginning to employ the reverse osmosis technology to improve the quality of fresh drinking water. Like every energy dependent industry, it is essential for energy to be effectively and efficiently utilized in this emerging sector of the economy so that the proprietors of the industry would be able to operate sustainably and provide potable drinking water to the teaming masses at affordable prices.

Viable water processing industries in various countries is paramount to meeting the Millennium Development Goals, which includes reducing by half the proportion of people without access to safe drinking water and basic sanitation in the second decade of the 21st century. The World Health Organization (WHO) and the United Nations Children's Fund (UNICEF) reported in 2012 that about 780 million people around the world lack access to clean drinking water [2]. Availability of fresh drinking water sources is regularly becoming an important issue, especially in regions with limited amount of water [3]. It was discovered that in China, close to 80% of major rivers are so degraded that they no longer support aquatic life, while 90% of the groundwater is contaminated, and less than 25% of the population of Pakistan has access to clean drinking water [4]. About half of the water in drinking water supply systems in the developing world is lost to leakage, illegal hookups, and vandalism [5]. Over 75 % of all diseases in developing countries are attributed to the consumption of polluted water or the lack of sanitary installation [6]. Accessibility to fresh clean water is required to interrupt the transmission of trachoma, the leading infectious cause of blindness worldwide [7].

Energyanalyses have been used by several researchers to analyze industrial plants and systems, such as, the performance of hybrid photovoltaic thermal air collector systems; malt drink production and fruit juice processing industries; system components of a steam power plant; and steam production and distribution system including alternatives to throttling and the single pressure steam production [8-12]. Energy balance is a means to quantitatively interpret a thermodynamic analysis based on the first law of thermodynamics. Energy efficiency is a useful decision making tools for thermodynamic processes. Energy analysis along with exergy studies usually helps to point to possible areas requiring improvement and enhanced performance of energy systems [13]. Most researches only studied the reverse osmosis system and units directly involved in processing of the feed stream, and not the entire processing plant [14-16]. Subsequently, any industry involved in water purification processes must seek to improve the performance of the entire industrial-value chain in other areas of units' operations.

Previous studies on water purification processing plants only focused on the first and second law efficiencies analysis, and never really pay attention on alternative use of energy sources and possible implications on the environment and cost of operation. This study focuses on energy analysis of a reverse osmosis water purification plant in order to determine means to efficiently utilize energy in the provision of portable drinking water. Furthermore, to find ways of minimizing operational cost, air pollution and emissions respectively.

II. DESCRIPTION OF THE REVERSE OSMOSIS (RO) WATER PROCESSING PLANT

The study was conducted at university of Ilorin water processing factory located in Ilorin, Nigeria. The facility employs a reverse osmosis technology for water purification. There are eleven major operating units involved in the entire plant to produce clean water fit for drinking as shown in Fig. 1 and Table 1. The plant utilizes a submersible pump capable of operating optimally continuously for about 5-7 hours at a time. Aside of purifying the water, other processes undertaken by the plant in the post purification processes, include washing and blowing of water bottles, filling and capping, batch coding and packaging respectively. The machines used for the post-water purification processes are included in Table 1. Raw bore-hole water is usually pumped from beneath the ground surface via a submersible pump, and stored in overhead tanks of 5000 liters' capacity each. The submersible pump was capable of delivering up to 5000 liters of water in 1.5 hours, which is at a rate of 3,333.33 liters/hour at peak operating conditions. Additives are added to the stored water before further processing in order to help disinfect the raw water. The water was passed through composites (sand composite and carbon composite). The sand composite helps in removing sand and stones in the water while the carbon composite helps to remove odor and also improve the appearance. The water was then passed through ultra-filters placed in the path of flow of the disinfected water. The water was then stored in treated tanks. The treated water was further passed through an ultra-filter. The entire process described above occurs outdoor.

The outdoor water was pumped from the treated tank to the reverse osmosis (RO) system via an ultra-filtration system. Clean water was then separated from salts and other contaminants which are either retained or rejected. The water leaving the RO system was further treated by an ultraviolet radiation ozonizer (UV-type ozone generator). The ozonation process involves ozone to form oxides with iron, manganese, and sulphur in the water to produce insoluble metal oxides or elemental sulphur particles which are then removed by post-filtration [17]. The clean purified water was stored in a storage tank, ready for packaging prior to consumption.

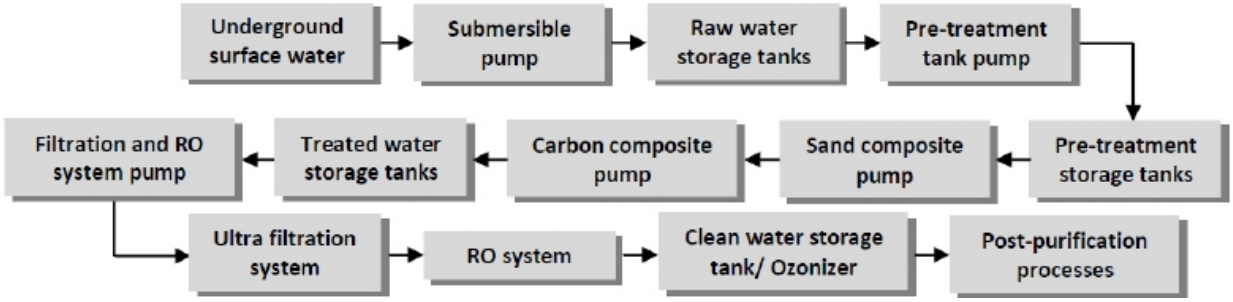

Fig. 1. Flow diagram for the reverse osmosis water processing plant.

III. METHOD

A. Data collection

Vital information required for conducting a detailed energy analysis of the plant were collected by direct investigation of the plant and inquisition of the plant personnel and other secondary sources. The data included operating units; rated power; operating efficiency; operating temperatures; generator specification, etc. associated with the plant operation as presented in Tables 1 and 2 respectively.

Operating units	Rated power (kW)	Operating efficiency (%)	Average operating temperature (°C)
1. Submersible pump	0.75	80	60.00
2. Pre-treatment tank pump	0.75	80	75.00
3. Sand composite pump	0.75	80	75.00
4. Carbon composite pump	0.75	80	75.00
5. Filtration and RO system pump	1.50	80	75.00
6. RO system	1.50	90	25.00
7. Ozonizer	0.14	90	30.00
8. Washing and blowing machine	0.55	75	45.00
9. Filling and capping	0.75	80	65.00
10. Batch coding machine	1.00	90	40.00
11. Packaging machine/compressor	1.50	80	210.00

Table 1. Operational parameters of operating units of the plant.

Property specification	Value
Depth of well	55.05 m
Distance from well location to raw water storage tanks	51.21 m
Inlet pressure of RO system	0.25 MPa
Flow rate of RO system	1000 kg/h
Generator rating	110 kVA
Generator motor efficiency	80%
Generator load during operation	60-70%
Generator fuel	Diesel
Rate of fuel consumption	11.43 litres/h
Operation time	7 hours
Calorific value of diesel fuel	35.70 kJ/litre
Electrical power factor	0.80

Table 2. Some related data of the operating plant.

B. Analytical method

1. Energy analysis of operating units and the plant

The output power of each operating unit of the plant can be obtained from their respective operating or energy efficiency and rated power which is taken as the input power to the units as presented in Table 1. The output powers for the operating units were determined by:

$$\eta_{op} = \frac{P_{out}}{P_{in}} \qquad (1)$$

where, η_{op} = operating efficiency, P_{out} = output power, and P_{in} = input power.

Subsequently, the input and output energy of each operating unit is expressed by Eqns. (2) and (3) as follows:

$$E_{in} = P_{in} \cdot t \cdot f \qquad (2)$$

$$E_{out} = \eta_{op} \cdot P_{in} \cdot t \cdot f \qquad (3)$$

where, t and f are the time in seconds and power factor respectively.

The energy efficiency of the plant can therefore be obtained by Eqn. (4):

$$\eta_{plant} = \frac{\sum E_{out}}{\sum E_{in}} \times 100\% \qquad (4)$$

2. Energy transfer analysis of the plant generating set

The output power of the generating set was determined as follows:

$$\eta_{gen} = \frac{W_{out}}{W_{in}} \qquad (5)$$

$$W_{in} = \frac{V \cdot I \cdot \sqrt{3} \cdot F \cdot L \cdot t}{1000} = \frac{kVA \cdot \sqrt{3} \cdot F \cdot L \cdot t}{1000} \; MJ/day \qquad (6)$$

where, η_{gen} is the generator motor efficiency; W_{in} and W_{out} are the inlet and output power in MJ/day of the generator; V · I is the product of voltage and current, which equals the kVA of the generator; F is the power factor; L is the generating load (≈ 65%); and t in seconds is the operation time in seconds. Therefore, the efficiency of energy transferred to the plant from the generator is given by:

$$\eta_{gen-plant} = \frac{\sum E_{in}}{W_{out}} \qquad (7)$$

3. Emission analysis of the plant generating set

The horsepower of the generating set can be determined as:

$$HP = \frac{kVA \times 1000}{746 \times \eta_{gen}} \qquad (8)$$

Hence, by making use of the Engine Air Emissions Calculator for Small Business Environmental Assistance Program (SBEAP) [19], and the values of the generator horsepower and operating hours, the Potential to Emit and Actual Emissions Calculations were obtained.

IV. RESULTS AND DISCUSSION

A. Energetic performances of the processing plant

The operational parameters of operating units of the water purification processing plant presented in Table 2, namely: rated power, operating efficiency, operating temperature were used in conjunction with Eqns. (1) to (4) for the energy performance analysis of the plant. The energy input and output of 15.12 and 12.12 MJ were respectively obtained for the submersible pump, pre-treatment tank pump, sand composite pump, and the carbon composite pump. The equivalent values of the input and output energy of these operating units was as a result of similarity in values of their rated power (0.75 kW) and operating efficiency (80%) accordingly. The highest input energy of 30.24 MJ was obtained for the filtration and RO system pump, RO system and packaging machine/compressor operating units due to the same values of their rated horse power (1.5 kW). The Ozonizer has the lowest input and output energy of 2.82 and 2.54 MJ because it possesses the lowest value of rated horsepower (0.14 kW). The overall input and output energy of the plant were determined as 200.39 and 165.08 MJ, and consequently the energy efficiency of the plant was obtained as 82.38%. The efficiency of energy transferred to the plant from the generator was determined as 10.01%. This implies that the capacity of generator required to supplement the energy requirement of the plant is only about 10% of the current capacity, that is, just 11 kVA generating set.

If about 15% of electrical energy is required for office operation and miscellaneous uses, then the actual capacity of supplementary generator required to run the entire plant and secondary energy demands would be 25% of current capacity or 27.5 kVA generating set. Furthermore, if a solar energy source is employed to power all the pumps of the plant and most of the office lightings and other accessories up to 50% of the initial 15%; the total energy input of the pumps to the total energy input of the plant would be 90.72 MJ: 200.39 MJ, that is 45.27%. Hence, employing a solar energy source can reduce the total energy of the plant facility by as much as 50%, leading to a required supplementary generator of only 13.75 kVA instead of the currently used 110 kVA, that is, 12.5% of the current capacity.

B. Emission and greenhouse gas generation of the processing plant

The emission and greenhouse gas generation of the processing plant was analyzed by mainly investigating the operation of the generating set employed as an auxiliary electricity power source to ensure continuous source of power to the plant when electricity outage is experienced from the national grid. Results of the greenhouse gas (GHG) emission and carbon dioxide equivalents (CO_2e) analysis of the generating set at average operating hours of 1092 hr/yr are presented in Tables 3 and 4. The generator rating of 110 kVA, equivalent to 184.32 hp accounted for the potential to emit and actual emissions of the

pollutant shown in Tables 3 and 4. At the current usage, the generating set produces actual emissions of CO_2 (114.864 tons/yr), CH4 (0.116 tons/yr) and N_2O (0.277 tons/yr) respectively; resulting in GHG total (CO_2e) of 115.258 tons/yr It had been demonstrated in above analysis that the actual capacity of generating set for the entire plant facility is only 13.75 kVA instead of the currently used 110 kVA. Using the horsepower equivalent of 13.75 kVA (23.04 hp) and estimated operating hours of 1092 hr/yr, the reduced values of actual emissions are obtained as: CO_2 (14.358 tons/yr), CH_4 (0.015 tons/yr) and N_2O (0.035 tons/yr) respectively; resulting in GHG total (CO_2e) of 14.407 tons/yr This shows a reduced value in GHG total (CO_2e) of 12.5% of the initial of the initial 115.258 tons/yr In otherwise, the GHG total (CO_2e) have been mitigated by 87.5% when appropriate energy transfer efficiency and solar energy source was considered. Also the potential to emit was reduced from 924.593 to 115.574 tons/yr for the GHG total (CO_2e).

Pollutant	Emission Factor (lb/hp·hr)	Emission Rate (lb/hr)	Potential to Emit (tons/yr)	Actual Emissions (tons/yr)
PM	0.0022	0.406	1.776	0.221
PM10	0.0022	0.406	1.776	0.221
S0x	0.00205	0.378	1.655	0.206
N0x	0.031	5.714	25.027	3.120
VOC	0.002514	0.463	2.030	0.253
CO	0.00668	1.231	5.393	0.672
Lead	-	-	-	-

Table 3. Emission analysis of the generating set operation at an average of 1092 hr/yr

Pollutant	Global Warming Potential	Emission Factor (lb/ hp·hr)	Emission Rate (lb/hr)	Potential To Emit (ton/yr)	Actual Emissions (ton/yr)
CO_2	1	1.14135	210.374	921.437	114.864
CH4	25	0.00004627	0.009	0.934	0.116
N_2O	298	0.00000924	0.002	2.223	0.277
GHG Total (CO_2e)				924.593	115.258

Table 4. Green House Gas (GHG) Emissions and (CO_2e) analysis.

Co_2e = carbon dioxide equivalents

V. CONCLUSION

The study involves the investigation of energy analysis of a water purification processing plant. The plant utilizes a supplementary energy source from a diesel generator to guarantee constant electricity supply whenever power outage is experienced from the national grid. The operating units with rated power of 0.75 kW and operating efficiency of 80% resulted in energy input and output of 15.12 and 12.12 MJ respectively. The overall input and output energy of the plant was obtained as 200.39 and

165.08 MJ, resulting in energy efficiency of the plant of 82.38%.The actual capacity of electrical generator required to supplement the energy requirement of the plant operation was determined to be only about 10% of the current capacity, that is, 11 kVA instead of 110 kVA. If solar energy is employed to power the pumps in the plant, and at the same time employing an optimum energy transfer from supplementary generating set to the plant facility (main plant, office equipment, etc.), a supplementary generator of only 13.75 kVA would be needed for the entire plant and other facilities instead of the currently used 110 kVA, which is just 12.5% of the current capacity. The use of an electrical generator is an issue of concern as far as a sustainable environment is concerned. Hence, it is necessary to find ways of mitigating the consequences of using a fossil fuel energy source. Furthermore, the greenhouse gas (GHG) emission and carbon dioxide equivalents (CO2e) of the generating set at an average operating hours of 1092 hr/yr and generator rating of 110 kVA (184.32 hp), resulted in GHG total (CO2e) of 115.258 tons/yr. The GHG total (CO2e) was found to reduce to 14.407 tons/yr when the horsepower equivalent of 13.75 kVA (23.04 hp) generating set was considered to replace the current 110 kVA (184.32 hp) generator.

Consequently, the study has shown that a sustainable environment could be enhanced by improving the energy transfer efficiency from energy sources to energy utility plants and by employing solar energy sources to replace fossil based energy sources for some of the plant operating units where possible. Also, overall energy efficiency of a plant can further be enhanced by a detailed energy and exergy analysis of individual operating units that makes up the plant in order to identify the machines with highest inefficiencies for possible redesign or technical replacement.

ACKNOWLEDGEMENTS

The authors hereby express their profound gratitude to the management and staff of the University of Ilorin water processing plant for their cooperation during the assessment of the plant and for providing relevant information used to conduct this study.

REFERENCE

[1] A. Opel, From water crisis to water culture, cultural studies, Taylor and Francis 22 (3-4) (2008) 498-509.
[2] T. Salaam-Blyther, Global access to clean drinking water and sanitation: U.S. and international programs. CRS Report for congress: Congressional Research Service, 2012.
[3] M. Cresswell, G. Naser, A water resources management strategy for small water districts-a case study of the south east Kelowna irrigation district, Can. J. Civ. Eng. 40 (2013) 499–507.
[4] M. Barlow, The growing movement to protect the global water commons, Brown Journal of World Affairs 17 (1) (2010) 181-195.
[5] A.S. Roberts, Technology: New ways for clean water, Resources in Technology and Engineering, Technology and Engineering Teacher, 2012.
[6] M. Rumberger, The availability of drinking water in the future-the disposal of sufficient drinking water in the long term range and the influence of the global change in climate, The Mineral Processing for a Sustainable World (2009) 64-68.

[7] M. Rog, B. Swenor, L.C. Cajas-Monson, W. Mchiwe, S. Kiboko, H. Mkocha, S. West, A cross-sectional survey of water and clean faces in trachoma endemic communities in Tanzania, BMC Public Health 11 (2011) 495.

[8] A.S. Joshi, I. Dincer, B.V. Reddy, Analysis of energy and exergy efficiencies for hybrid PV/T systems, International Journal of Low-Carbon Technologies 6 (2010) 64-9.

[9] D.A. Fadare, D.O. Nkpubre, A.O. Oni, A. Falana, M.A. Waheed, O.A. Bamiro, Energy and exergy analyses of malt drink production in Nigeria, Energy 35 (2010) 5336-5546.

[10] M. A. Waheed, S. O. Jekayinfa, J. O. Ojediran, O. E. Imeokparia, Energetic analysis of fruit processing in Nigeria, Energy 33 (2008) 35-45.

[11] I.H. Aljundi, Energy and exergy analysis of a steam power plant in Jordan, Applied Thermal Engineering 29 (2009) 324-328.

[12] A.B. Rian, I.S. Ertesvag, Exergy analysis of a steam production and distribution system including alternatives to throttling and the single pressure steam production, Energy Conversion and Management 52 (2011) 703-712.

[13] R.A. Dias, J.A.P. Balestieri, Energetic and exergetic analysis in a firewood boiler, Revista De Ciencia and Tecnologia 12 (23) (2004) 15-24.

[14] M.H. Sharqawy, S.M. Zubair, J.H. Lienhard-V, Second law analysis of reverse osmosis desalination plants: an alternative design using pressure retarded osmosis, Energy 36 (2011) 6617-6626.

[15] Y. Cerci, Exergy analysis of a reverse osmosis desalination plant in California, Desalination 142 (2002) 257-66.

[16] I.H. Aljundi, Second-law analysis of a reverse osmosis plant in Jordan, Desalination 239 (2009) 207-215.

[17] K.K. Patel, S.J. Patel, T.S. Patel, H.J. Patel, J.G. Patel, A. Sinha, D.J. Sen, Mineral water as a trust, quality, taste and worth for the elixir of life, European Journal of Biomedical and Pharmaceutical Sciences 4 (2) (2017) 136-148.

[18] Y. Demirel, Thermodynamic Analysis, Arab J SciEng 38 (2013) 221-249.

[19] Small Business Environmental Assistance Program (SBEAP), Engine Air Emissions Calculator [online], MN Small Business Environmental Assistance Program. Accessed: 3rd August, 2018. www.pca.state.mn.us/sbeap

Instructions for Authors

Essentials for Publishing in this Journal

1 Submitted articles should not have been previously published or be currently under consideration for publication elsewhere.

2 Conference papers may only be submitted if the paper has been completely re-written (taken to mean more than 50%) and the author has cleared any necessary permission with the copyright owner if it has been previously copyrighted.

3 All our articles are refereed through a double-blind process.

4 All authors must declare they have read and agreed to the content of the submitted article and must sign a declaration correspond to the originality of the article.

Submission Process

All articles for this journal must be submitted using our online submissions system. http://enrichedpub.com/ . Please use the Submit Your Article link in the Author Service area.

Manuscript Guidelines

The instructions to authors about the article preparation for publication in the Manuscripts are submitted online, through the e-Ur (Electronic editing) system, developed by **Enriched Publications Pvt. Ltd**. The article should contain the abstract with keywords, introduction, body, conclusion, references and the summary in English language (without heading and subheading enumeration). The article length should not exceed 16 pages of A4 paper format.

Title

The title should be informative. It is in both Journal's and author's best interest to use terms suitable. For indexing and word search. If there are no such terms in the title, the author is strongly advised to add a subtitle. The title should be given in English as well. The titles precede the abstract and the summary in an appropriate language.

Letterhead Title

The letterhead title is given at a top of each page for easier identification of article copies in an Electronic form in particular. It contains the author's surname and first name initial .article title, journal title and collation (year, volume, and issue, first and last page). The journal and article titles can be given in a shortened form.

Author's Name

Full name(s) of author(s) should be used. It is advisable to give the middle initial. Names are given in their original form.

Contact Details

The postal address or the e-mail address of the author (usually of the first one if there are more Authors) is given in the footnote at the bottom of the first page.

Type of Articles

Classification of articles is a duty of the editorial staff and is of special importance. Referees and the members of the editorial staff, or section editors, can propose a category, but the editor-in-chief has the sole responsibility for their classification. Journal articles are classified as follows:

Scientific articles:

1. Original scientific paper (giving the previously unpublished results of the author's own research based on management methods).

2. Survey paper (giving an original, detailed and critical view of a research problem or an area to which the author has made a contribution visible through his self-citation);

3. Short or preliminary communication (original management paper of full format but of a smaller extent or of a preliminary character);

4. Scientific critique or forum (discussion on a particular scientific topic, based exclusively on management argumentation) and commentaries. Exceptionally, in particular areas, a scientific paper in the Journal can be in a form of a monograph or a critical edition of scientific data (historical, archival, lexicographic, bibliographic, data survey, etc.) which were unknown or hardly accessible for scientific research.

Professional articles:

1. Professional paper (contribution offering experience useful for improvement of professional practice but not necessarily based on scientific methods);
2. Informative contribution (editorial, commentary, etc.);
3. Review (of a book, software, case study, scientific event, etc.)

Language

The article should be in English. The grammar and style of the article should be of good quality. The systematized text should be without abbreviations (except standard ones). All measurements must be in SI units. The sequence of formulae is denoted in Arabic numerals in parentheses on the right-hand side.

Abstract and Summary

An abstract is a concise informative presentation of the article content for fast and accurate Evaluation of its relevance. It is both in the Editorial Office's and the author's best interest for an abstract to contain terms often used for indexing and article search. The abstract describes the purpose of the study and the methods, outlines the findings and state the conclusions. A 100- to 250-Word abstract should be placed between the title and the keywords with the body text to follow. Besides an abstract are advised to have a summary in English, at the end of the article, after the Reference list. The summary should be structured and long up to 1/10 of the article length (it is more extensive than the abstract).

Keywords

Keywords are terms or phrases showing adequately the article content for indexing and search purposes. They should be allocated heaving in mind widely accepted international sources (index, dictionary or thesaurus), such as the Web of Science keyword list for science in general. The higher their usage frequency is the better. Up to 10 keywords immediately follow the abstract and the summary, in respective languages.

Acknowledgements

The name and the number of the project or programmed within which the article was realized is given in a separate note at the bottom of the first page together with the name of the institution which financially supported the project or programmed.

Tables and Illustrations

All the captions should be in the original language as well as in English, together with the texts in illustrations if possible. Tables are typed in the same style as the text and are denoted by numerals at the top. Photographs and drawings, placed appropriately in the text, should be clear, precise and suitable for reproduction. Drawings should be created in Word or Corel.

Citation in the Text

Citation in the text must be uniform. When citing references in the text, use the reference number set in square brackets from the Reference list at the end of the article.

Footnotes

Footnotes are given at the bottom of the page with the text they refer to. They can contain less relevant details, additional explanations or used sources (e.g. scientific material, manuals). They cannot replace the cited literature.
The article should be accompanied with a cover letter with the information about the author(s): surname, middle initial, first name, and citizen personal number, rank, title, e-mail address, and affiliation address, home address including municipality, phone number in the office and at home (or a mobile phone number). The cover letter should state the type of the article and tell which illustrations are original and which are not.

Address of the Editorial Office:

Enriched Publications Pvt. Ltd.
S-9,IInd FLOOR, MLU POCKET,
MANISH ABHINAV PLAZA-II, ABOVE FEDERAL BANK,
PLOT NO-5, SECTOR -5, DWARKA, NEW DELHI, INDIA-110075,
PHONE: - + (91)-(11)-45525005